Mineral Sequestration of Carbon Dioxide in a Sandstone-Shale System

Tianfu Xu, John A. Apps, and Karsten Pruess

Earth Sciences Division, Lawrence Berkeley National Laboratory
University of California, Berkeley, CA 94720, USA

Abstract. A conceptual model of CO_2 injection in bedded sandstone-shale sequences has been developed using hydrogeologic properties and mineral compositions commonly encountered in Gulf Coast sediments. Numerical simulations were performed with the reactive fluid flow and geochemical transport code TOUGHREACT to analyze mass transfer between sandstone and shale layers and CO_2 immobilization through carbonate precipitation. Results indicate that most CO_2 sequestration occurs in the sandstone. The major CO_2 trapping minerals are dawsonite and ankerite. The CO_2 mineral-trapping capacity after 100,000 years reaches about 90 kg per cubic meter of the medium. The CO_2 trapping capacity depends on primary mineral composition. Precipitation of siderite and ankerite requires Fe^{+2} supplied mainly by chlorite and some by hematite dissolution and reduction. Precipitation of dawsonite requires Na^+ provided by oligoclase dissolution. The initial abundance of chlorite and oligoclase therefore affects the CO_2 mineral trapping capacity. The sequestration time required depends on the kinetic rate of mineral dissolution and precipitation. Dawsonite reaction kinetics is not well understood, and sensitivity regarding the precipitation rate was examined. The addition of CO_2 as secondary carbonates results in decreased porosity. The leaching of chemical constituents from the interior of the shale causes slightly increased porosity. The limited information currently available for the mineralogy of natural high-pressure CO_2 gas reservoirs is also generally consistent with our simulation. The "numerical experiments" give a detailed understanding of the dynamic evolution of a sandstone-shale geochemical system.

Key words. CO_2 sequestration, numerical simulation, mineral trapping, bedded sandstone-shale.

1. Introduction

A possible means of reducing carbon dioxide (CO_2) emissions to the atmosphere is injection of CO_2 into structural reservoirs in deep permeable geologic formations (Holloway, 1997). Such formations could include aquifers, oil and gas fields, and coal seams. Aquifers are the most abundant fluid reservoirs in the subsurface. The deepest aquifers in the United States commonly contain brackish or saline water. Aquifers with salinities exceeding 10,000 mg/L total dissolved solids are excluded by the U.S. Environmental Protection Agency as underground sources of drinking water. Hence, they are logical targets for the eventual disposal of CO_2. The feasibility of storing CO_2 in aquifers has been discussed in the technical literature over the last decade. These include an evaluation of the feasibility of CO_2 aquifer storage in The Netherlands (Lohuis, 1993) and in the Alberta Basin, Canada (Gunter et al., 1993, Bachu et al., 1994, Perkins and Gunter, 1995; Law and Bachu, 1996, Gunter et al., 1996 and 1997). Furthermore, large-scale CO_2 disposal in an aquifer is already being practiced in the Norwegian sector of the North Sea (Korbol and Kaddour, 1995). Recently, extensive experimental, field, and modeling studies of geological carbon sequestration have been conducted (Pearce et al., 1996; Rochelle et al., 1996; Gunter et al., 1997; Ortoleva et al., 1998; Johnson et al., 2001; White et al., 2001; McPherson and Lichtner, 2001; Oelkers et al., 2002; Rosenbauer, and Koksalan, 2002; Kaszuba, et al., 2002; Boram, et al., 2002; Matter et al., 2002; Giammar et al., 2002; Jones et al., 2002; Goodman, et al., 2002; Hedges et al., 2002; Hovorka, et al, 2002; Horita, J., 2002; Knauss et al., 2002; Solano-Acosta et al., 2002; Palandri and Kharaka, 2002; Strazisar and Zhu, 2002; Perkins et al, 2002; Pruess et al., 2003).

Numerical modeling of geochemical processes is necessary to investigate long-term CO_2 injection in deep aquifers, because aluminosilicate mineral alteration is very slow under ambient deep-aquifer conditions and is not amenable to experimental study. Xu et al. (2004) present a geochemical modeling analysis of the interaction of aqueous solutions under high CO_2 partial pressures with three different rock types. The first rock is a glauconitic sandstone from the Alberta Sedimentary Basin. The second rock type

evaluated is a proxy for a sediment from the United States Gulf Coast. The third rock type is a dunite, an essentially monomineralic rock consisting of olivine.

Xu et al. (2003) performed reactive transport simulations of a 1-D radial well region under CO_2 injection conditions in order to analyze CO_2 immobilization through carbonate precipitation, using Gulf Coast sandstones of the Frio formation of Texas. Most of the simulated mineral alteration pattern is consistent with the observations. Some inconsistencies with field observations are noted. For example, quartz abundance declines over the course of the simulation, while quartz overgrowths are observed during diagenesis due to the release of SiO_2 during replacement of smectite by illite in adjacent shales (Land, 1984). The formation of pyrite in the field is not reproduced by the previous simulation, because sulfur (S) was not included in the kerogen composition.

The previous modeling (Xu et al., 2003 and 2004) was simplified and approximated many of the complexities of actual diagenesis in the field. Major simplifications and limitations include, (1) treating the sandstone aquifer as if it were a closed system isolated from the enclosing shales, and (2) not adequately representing the extremely complex process of kerogen decomposition (or petroleum maturation) in deeply buried sediments. The proportions of reactant minerals in the simulation therefore differ from that of the total system in the field. The long-term interaction of injected carbon dioxide into sandstone aquifers with shale confining layers has not yet been investigated.

Here we present simulation results on mass transfer, mineral alteration, and consequent CO_2 sequestration by carbonate precipitation in a sandstone-shale system. The mineral compositions of sandstone and shale were taken from Gulf Coast sediments. The mineralogy, thermodynamic database and kinetic data are refined from previous studies (Xu et al., 2003 and 2004).

2. Numerical Modeling Approach

2.1. Simulation method

The present simulations were carried out using the non-isothermal reactive geochemical transport code TOUGHREACT (Xu and Pruess, 1998 and 2001). This code was developed by introducing reactive chemistry into the framework of the existing multi-phase fluid and heat flow code TOUGH2 (Pruess et al., 1999). Our modeling of flow and transport in geologic media is based on space discretization by means of integral finite differences (Narasimhan and Witherspoon, 1976). An implicit time-weighting scheme is used for the individual components of the model consisting of flow, transport, and kinetic geochemical reactions. TOUGHREACT uses a sequential iteration approach similar to that of Yeh and Tripathi (1991). After solution of the flow equations, the fluid velocities and phase saturations are used for chemical transport simulation. The chemical transport is solved on a component basis. The resulting concentrations obtained from the transport are substituted into the chemical reaction model. The system of chemical reaction equations is solved on a grid-block basis by Newton-Raphson iteration, similar to those by Parkhurst et al. (1980), Reed (1982), and Wolery (1992). The chemical transport and reactions are iteratively solved until convergence. Full details on the numerical methods are given in Xu and Pruess (1998, 2001).

2.2. Process capabilities

The simulator can be applied to one-, two-, or three-dimensional porous and fractured media with physical and chemical heterogeneity, and can accommodate any number of chemical species present in liquid, gas and solid phases. A wide range of subsurface thermo-physical-chemical processes is considered. The major processes considered for fluid and heat flow are: (1) fluid flow in both liquid and gas phases under pressure and gravity forces, (2) capillary pressure effects for the liquid phase, and (3) heat flow by conduction, convection and diffusion.

Transport of aqueous and gaseous species by advection and molecular diffusion is considered in both liquid and gas phases. Hydrodynamic dispersion is an important solute

transport mechanism that arises from an interplay between non-uniform advection and molecular diffusion. The process is often represented by a Fickian diffusion analog (convection-dispersion equation) that has fundamental flaws and limitations, details on dispersion are discussed in Xu and Pruess (2001). A Fickian model for dispersion is not used in TOUGHREACT. Instead, hydrodynamic dispersion is modeled through appropriate spatial resolution on multiple scales. In any case, the fluid velocity in the present problem is very low.

Aqueous chemical complexation and gas (CO_2) dissolution and exsolution are assumed to be locally at equilibrium. Mineral dissolution and precipitation can be modeled subject to either local equilibrium or kinetic conditions. The kinetic rate law used is given in Section 2.4. The activity of aqueous species is equal to the product of the activity coefficient and molal concentration (mol/kg H_2O). Aqueous species activity coefficients with the exception of CO_2(aq) are calculated from the extended Debye-Hückel equation (Helgeson et al., 1981). CO_2(aq) activity coefficient and CO_2(g) fugacity coefficient are functions of pressure, temperature and salinity (details on calculations are given in Xu et al., 2004). The so-called "oxygen approach" is used for formulating redox reactions, which relates the oxidation potential to the activity of dissolved oxygen (Nordstrom and Muñoz, 1986; Wolery, 1992).

Changes in porosity and permeability due to mineral dissolution and precipitation can modify fluid flow. This feedback between flow and chemistry can be important and is considered in our model. Changes in porosity during the simulation are calculated from changes in mineral volume fractions. A simple Kozeny-Carman grain model based on spheres was used to calculate changes in permeability due to changes in porosity. The porosity-permeability correlation in geologic media depends on a complex interplay of many factors, such as pore size distribution, pore shapes, and connectivity (Verma and Pruess, 1988). Additional porosity-permeability relationships will be considered in the future. Because diffusion is the main transport process for CO_2 delivery to the shale from sandstone, the permeability correction is not important for the present simulation.

2.3. Thermodynamic data

The quality and accuracy of geochemical modeling is enhanced through the use of internally consistent and critically evaluated thermodynamic data derived from a comprehensive review of the published literature. The primary source for equilibrium constants for aqueous species and minerals used in this study originated with the EQ3/6 V7.2b database (Wolery, 1992). However, many substitutions and changes have been incorporated in response to more recent published revisions in the thermodynamic properties of several rock forming minerals and aqueous species. Among these are revisions to the feldspars by Arnorsson and Stefansson (1999), several clay minerals by Kulik and Aja (1997), and dawsonite (Ferrante et al., 1976). In addition, a comprehensive revision to the properties of silica polymorphs and SiO_2(aq) was initiated as a result of a recent refinement by Rimstidt (1997) of the low temperature aqueous solubility of quartz. Revised thermodynamic properties of relevant aqueous species based on the Helgeson-Kirkham-Flowers (HKF) equation of state (Shock et al., 1997), including aluminum species were also incorporated. Changes in the properties of SiO_2(aq) and AlO_2^- necessitated recomputation of the solubility products for all minerals containing silica or alumina components, whose thermodynamic properties were based on calorimetric measurements.

To ensure consistency with unmodified equilibrium constants in the EQ3/6 V7.2b database, previously generated from thermodynamic data using SUPCRT92 (Johnson et al., 1992), all revised thermodynamic data were incorporated in the SUPCRT92 database and new equilibrium constants similarly generated.

In addition to the changes noted above, the thermodynamic properties of several other phases were estimated and their solubility products incorporated to improve model verisimilitude for this paper. Brief descriptions regarding the methods used to calculate their properties follow.

Carbonates

An essential requirement for reactive transport simulations involving CO_2 sequestration is the need for accurate thermodynamic data of participating carbonate

phases. Recent studies have revealed the possible existence of substantial errors in the Gibbs free energy of formation of magnesite and dolomite (Rock et al., 2001). Furthermore, the experimental consistency of siderite solubility data (Preis and Gamsjager, 2002) has been recently established, and by inference, validated the thermodynamic data for ferrous and ferric ions recommended by Parker and Khodakovskii (1995). These modifications also require a redetermination of the thermodynamic properties of the ankerite solid solution utilized in earlier work (Xu et al., 2004).

The thermodynamic properties of dolomite and magnesite were calculated, using the Gibbs free energy values determined by Rock et al. (2001), together with the respective entropies provided by Robie and Hemingway (1995). These, together with entropy data for end-member ankerite, $CaFe(CO_3)_2$, from Holland and Powell (1998) and the properties of siderite from Preis and Gamsjager (2002) and calcite from the SUPCRT92 database, were used to calculate the properties of end-member ankerite and the ankerite ideal binary solid solution with the limiting composition: $CaMg_{0.3}Fe_{0.7}(CO_3)_2$, using the lattice energy calculations reported by Chai and Navrotsky (1996).

Chlorite

In prior simulations (Xu et al., 2004), chlorite was represented as a 1:1 mixture of clinochlore and daphnite. The solubility products used were those derived originally from the thermodynamic evaluation of phase equilibria by Helgeson et al. (1978). More recent and more comprehensive evaluations, e.g., that conducted by Holland and Powell (1998) indicate that a revision in the thermodynamic properties of clinochlore and daphnite is called for. Chlorite is only a minor phase in Gulf Coast shales and sandstones. However, chlorite competes with secondary carbonates for magnesium and ferrous iron. Furthermore, the simulation would be more representative if a chlorite solid solution, corresponding to that of ripidolite, were to be included in the reactant minerals of the simulation rather than being represented by a mixture of the end members.

The calculated thermodynamic properties for clinochlore and daphnite were taken from Holland and Powell (1998), and those for chlorite, $Mg_{2.5}Fe_{2.5}Al_2[Si_3O_{10}](OH)_8$,

were calculated assuming ideal solid solution between the end members. Thermodynamic properties for both end members of the solid solution were entered into the SUPCRT92 database, retaining the original Maier-Kelly heat capacity function and the ripidolite solubility products recalculated for entry in the TOUGHREACT database.

Kerogen-OS

Field observations suggest that an important consequence of kerogen maturation is the reduction of ferric iron to ferrous ion (Lynch, 1997) and the formation in small amounts of ubiquitous, secondary pyrite. The sulfur could originate from one or more sources including introduction with connate seawater, the dissolution of distal evaporite beds, biogenic reduction of dissolved sulfate contemporaneous with organic entrapment in accumulating seafloor sediments, or from thiol groups in kerogen itself. The fate of iron in the system during diagenesis is affected by competition between HS^- and HCO_3^- for the formation respectively of pyrite and ferrous carbonates at elevated CO_2 partial pressures during CO_2 sequestration. Preliminary closed system model simulations revealed that the quantity of sulfur would be insufficient were it to be present only in the pore water, and if derived from connate seawater. Furthermore, specified closed-system conditions precluded exogenous introduction through the dissolution of anhydrite or gypsum evaporites, even though this source could be significant in some field scenarios. We therefore refined our representation of kerogen oxygenated functional groups, -CHOH, -CHCOOH and -$CHCOOCH_2CH_3$ used in earlier modeling (Xu et al., 2004) through the addition of the thiol group. Although many different cross-linking sulfur-sulfur and sulfur-carbon bonds have been identified in type II kerogen, (e.g. see Hold et al., 1998), we decided, for simplicity, to incorporate sulfur simply as –CHSH. The sulfur was incorporated in the molar ratio O:S::4:1, which is approximately equivalent to the average ratio found in Type II kerogen analyses summarized by Tissot and Welte (1978, Table II.4.1). Thus the final composition of the kerogen functional groups, designated Kerogen-OS is $–(CHOH)_{18}(\text{-}CHCOOH)_5(\text{-}CHCOOCH2CH3)_6(\text{-}CHSH)_{10}$.

In computing the thermodynamic properties of the attached oxygenated functional groups, the molal properties (ΔG^o_f, ΔH^o_f, S^o, and the Maier-Kelley heat capacity function coefficients, *a*, *b*, *c*) of functional group components were taken from Helgeson et al.

(1998) and Richard and Helgeson (1998). The thermodynamic properties of –CHSH were calculated assuming that the difference between –CHOH and –CHSH was the same as the difference between liquid methanol, CH_3OH and liquid methanethiol, CH_3SH. Relevant data for methanethiol were taken from Russell et al. (1942) and Good et al. (1961), as summarized by NIST (http://webbook.nist.gov). For methanol, data were taken from Baroody and Carpenter (1970), Carlson and Westrum (1971), and for C_P, an average of 13 values given by NIST, (loc. cit.) from references between 1981 and 1992. Molar volume differences were calculated from density data given in the Handbook of Physical Chemistry. The computed thermodynamic properties of the oxygenated functional groups and –CHSH were summed and appropriate dissociation equilibria for kerogen-OS calculated using SUPCRT92 (Johnson et al., 1992).

Revision of Fe^{2+} and Fe^{3+}

Uncertainties relating to the thermodynamic properties of the ferrous and ferric ions in aqueous solution have bedeviled precise modeling of geochemical systems involving these species for some time, e.g. see Nordstom (1984) and Reardon and Beckie (1987). Recent work on the solubility of siderite (Preis and Gamsjager, 2002) provides support for the validity of the properties of Fe^{2+} in the survey by Parker and Khodakovskii (1995). We therefore incorporated revised properties of Fe^{2+} and Fe^{3+} in SUPCRT92 and recalculated the solubility products of all participating iron-containing minerals whose thermodynamic properties were derived from calorimetry. These included chlorite, daphnite, pyrite, and hematite, as well as appropriate corrections to the solubility products of siderite and ankerite.

2.4. Kinetic data

For kinetically-controlled mineral dissolution and precipitation, a general form of rate law (Lasaga, 1984; and Steefel and Lasaga, 1994) is used

$$r_m = \pm k_m A_m a_{H^+}^n \left| \left[\left(\frac{Q_m}{K_m} \right)^{\mu} - 1 \right] \right|^{\nu} \qquad (1)$$

where m is mineral index, r_m is the dissolution/precipitation rate (positive values indicate dissolution, and negative values precipitation), A_m is the specific reactive surface area per kg H_2O, k_m is the rate constant (moles per unit mineral surface area and unit time) which is temperature dependent, a_{H^+} is the activity of H^+ and n is empirical reaction order accounting for catalysis by H^+ in solution. K_m is the equilibrium constant for the mineral-water reaction written for the destruction of one mole of mineral m, Q_m is the reaction quotient, the parameters μ and ν are two positive numbers normally determined by experiment, and are usually, but not always, taken equal to unity (as in the present work). The temperature dependence of the reaction rate constant can be expressed reasonably well via an Arrhenius equation (Lasaga, 1984; and Steefel and Lasaga, 1994). Since many rate constants are reported at 25 ^oC (298.15 K), it is convenient to approximate rate constant dependency as a function of temperature, thus

$$k = k_{25} \exp\left[\frac{-E_a}{R}\left(\frac{1}{T} - \frac{1}{298.15}\right)\right] \qquad (2)$$

where E_a is the activation energy, k_{25} is the rate constant at 25 ^oC, R is gas constant, and T is absolute temperature.

Mineral dissolution and precipitation rates are a product of the kinetic rate constant and reactive surface area (Eq. 1). The parameters used for the kinetic rate expression are given in Table 1. Calcite is assumed to react at equilibrium because its reaction rate is typically quite rapid. In Table 1, we include the separate rate constant (k_{25}), the activation energy (E_a), and the reaction order (n) for each mechanism (acid catalyzed and no catalysis). At any pH the total rate is the sum of the rates via each mechanism. The acid catalysis is considered only for mineral dissolution. The temperature-dependent kinetic rate constants are calculated from Eq. 2. Some kinetic parameters were taken directly from the published scientific literature. The references are listed in the fifth column of Table 1. Others were set to the minerals with known kinetic properties. The evolution of surface area in natural geologic media is very complex,

especially for multi-mineralic systems, and is not quantitatively understood at present. Mineral reactive surface areas (last column of Table 1) were taken from Sonnenthal and Spycher (2001), which were calculated assuming a cubic array of truncated spheres that make up the framework of the rock. For clay minerals kaolinite, illite, and smectite, surface areas were increased to account for edges in these sheet silicate minerals (Nagy, 1995). The kinetic rate constants given in Table 1 were normalized to BET surface areas in the original studies. The geometric surface areas should be normalized to BET surface areas according to the roughness factor of individual minerals. A reactive surface area calculated from grain size may be a poor estimate of the hydrologically accessible mineral surface area. Furthermore, in multi-mineralic field scale systems the reactive surface area for a given mineral is generally smaller due to many factors such as coating. To account these effects, surface areas listed in Table 1 were arbitrarily reduced by one order of magnitude in the present simulations.

The precipitation of possible secondary minerals is represented using the same kinetic expression as that for dissolution. However, several aspects regarding precipitation are different from dissolution, including nucleation, crystal growth and Ostwald ripening processes, as well as the calculation of the reactive surface area (Steefel and van Capellen, 1990). These processes for mineral precipitation are not considered in the current model. The magnitudes of surface areas are highly uncertain and cover a wide range of values. Sensitivity regarding the kinetic rate constants and reactive surface areas are addressed later in this paper.

3. Problem Setup

3.1. Sandstone-shale configuration and properties

Much specific and detailed information will be required to assess the feasibility of disposing of CO_2 in a sandstone-shale formation at any particular site, and to develop engineering designs for CO_2 disposal systems. Before moving into site-specific investigations, general features and issues relating to the formation injection of CO_2 should be explored. This can be done by investigating a sandstone-shale system that

abstracts site-specific features representing characteristics that are common to many such systems.

A basic issue is the mass transfer and geochemical behavior in bedded sandstone-shale sequences under high-CO_2 pressure conditions. A simplified 1-D model of a sandstone-shale system is used (Figure 1). Hydrological parameter specifications for sandstone and shale layers were chosen to represent conditions encountered in Texas Gulf Coast sediments at a depth of order 2 km (Table 2). A porosity of 0.3 was used for sandstone based on Loucks et al. (1984), and a porosity of 0.1 for shale based on Howard (1991). Porosity may vary from sample to sample. Nevertheless, variations of porosity do not affect the mineral alteration pattern. The model grid is made finer in the shale near the interface between sandstone and shale to better resolve concentration gradients in the low permeability shale. Only one grid block was used for the sandstone layer and the calculation point for this block was placed at the interface. This represents a conceptual model of perfect mixing throughout the sand.

3.2. Mineralogy and geochemistry

A proxy for sandstone-shale sequences from the United States Gulf Coast was used to represent the mineralogy and geochemistry. The initial mineral composition of sandstone used in the present modeling (Table 2), was taken from Xu et al. (2004). The specification of formation mineralogy is determined in part by the availability of data. Most studies related to the Tertiary Gulf Coast sediments are concentrated in the state of Texas. The principal reservoir-quality sandstones within that region are found in the Frio, the Vicksberg and the Wilcox formations, all of which are Lower Tertiary age. Of the three formations, the Frio was chosen as a representative candidate for the sequestration of supercritical CO_2. It is the shallowest of the three formations, but over much of its areal extent, it is located at depths between 1,524 and 6,096 m, sufficient to ensure adequate CO_2 densities for effective storage.

Loucks et al. (1984) used the sandstone classification of Folk (1968) to describe sandstone reservoirs in the Lower Tertiary Gulf Coast sediments of Texas. This classification projects the composition of sandstones onto a ternary diagram in terms of the components: quartz, feldspar and rock fragments. For the purposes of this study, the

approximate mean composition of the Frio sandstone in the middle Texas region of the Gulf Coast was chosen. This composition is a representative of a quartzose lithic arkose with 56% quartz, 28% feldspar and 16% lithic fragments. According to Loucks et al. (loc. cit.), the lithic fragments in the Frio formation of this region are predominantly volcanic fragments, although significant percentages of metamorphic rocks are present. Carbonate rock fragments are also present in minor amounts. The volcanic fragments are believed to be mainly rhyolites and trachytes, which have been silicified or altered to chlorite. The carbonate fragments were apparently locally derived from adjacent landmass caliche soils. Neither the provenance nor the character of the metamorphic rocks is described.

The fractions of plagioclases and alkali feldspars making up the feldspar component, and the mineralogy of the lithic fragments are based on the work of Land (1984), who reports 1,634 electron probe point counts on 29 Frio formation rocks. About 30% of the original feldspar was K-feldspar and the remainder was plagioclase having an average anorthite (An) content of 20%. The composition of the lithic fragments has been described only qualitatively, and therefore, the actual mineral composition can only be surmised. Secondary minerals (calcite, clay minerals, and iron oxides) are not included in published lithological classifications. Therefore, the inclusion of these phases is based on subjective estimates. The observed presence of chlorite in lithic fragments of volcanic rock (Loucks et al., loc. cit.) is represented by 4.6 vol.% ripidolite. A small amount of hematite (0.5 vol.%) was added to take into account the presence of ferric iron staining. The concentrations of clay minerals, smectite, illite and kaolinite were arbitrarily assigned concentrations of 3.9, 1.0 and 2.0 vol.% respectively, and assigned as the residue of the mineral contribution by lithic fragments. The compositions of smectite and illite are those representative of I/S clays, typical of Gulf Coast sediments.

The model shale composition is based on the recent study by Land et al. (1997) of Upper Oligocene - Lower Miocene mudrocks obtained at depths between 2130 and 5490 m from the Mobil #406 State Tract well in Kenedy County, Texas. Neither the location, nor the provenance of the studied mudrocks corresponds closely with the selected model sandstone. The Mobil #406 State Tract well is located on the South Texas Gulf Coast whereas the sandstone composition was selected as representative of the mid Texas Gulf

coast (Loucks et al., 1984). However, the quality of the analytical and mineralogical analyses is believed to be superior to earlier, but potentially more representative analyses such as those by Hower et al. (1976), for the reasons cited by Land et al. (loc. cit.), and therefore are preferred.

The mineralogical analyses given in Table 1 of Land et al. (1997) were plotted versus depth, and linearly regressed to obtain a functional relation with depth. Not all trends were linear, and slightly better fits were obtained in some cases with second order polynomial equations despite the substantial scatter in the data. However, only the linear correlations were used, and these were extrapolated incrementally to a depth of 2,000 m, corresponding to an approximate ambient temperature of approximately 75 °C. The mineralogical concentrations (Wt.%) were converted to specific volumes (m^3/mol) and normalized to 98 vol.%, the balance of 2 vol.% being assigned to organic matter, i.e. kerogen-OS. In the process of making these calculations, some simplifications and assumptions were introduced to facilitate modeling. All plagioclase was assumed to have the composition of oligoclase (Table 3), chlorite was assumed to have a 1:1 clinochlore:daphnite composition, corresponding to ripidolite. Finally, the I/S was divided into separate illite and smectite components in accordance with the mineralogical compositions for I/S specified by Kulik and Aja (1997), and the illite component lumped with the detrital illite. The smectite component is assumed to be a sodium end member, as would be expected if in contact with a 1-molal solution of NaCl. These adjustments are considered realistic compromises in the light of current model development. The resulting mineralogical composition of the shale is presented in Table 3.

Prior to the reactive transport simulations in the sandstone-shale system, batch geochemical modeling of water-rock interaction for individual sandstone and shale was performed to obtain a nearly equilibrated water chemistry (see Table 4) using a pure 1.0 M solution of sodium chloride and CO_2 gas pressure (P_{CO2}) of 1×10^{-2} bar reacting with the primary minerals listed in Table 3 at a temperature of 75 ^{o}C. We chose $P_{CO2} = 10^{-2}$ bar at 75°C, to ensure that the pH of the pore water fell into the general range observed for Gulf Coast brines with a salinity of about 1.0 mol/L, e.g. see Kreitler and Richter (1986), rather than specifically attempting to replicate P_{CO2}. The resulting water chemistry (Table 4) was used for the initial condition of reactive geochemical transport simulations.

A separate supercritical CO_2 phase (called gas phase in this paper) is initially placed in the sandstone grid block with a gas phase saturation of 0.5 and a water saturation of 0.5. Whereas, the shale layer is initially water saturated. A CO_2 gas pressure of 201 bars is used in the simulation, which is close to hydrostatic pressure at a depth of 2 km. A temperature of 75^{o}C is used based on a land surface temperature of 15^{o}C and a geothermal gradient of 30^{o}C/km. The CO_2 gas phase is assumed to be in equilibrium with the aqueous phase at all times. The solubility of CO_2 in the aqueous phase depends on pressure, temperature, and salinity. The details on solubility calculations are given in Xu et al. (2004). The reactive geochemical transport simulations were performed for a period of 100,000 years.

The first simulation used parameters given in Tables 1 through 4, which we call base-case simulation. Mineral dissolution and precipitation rates are a product of the kinetic rate constant and reactive surface area, the magnitudes of which are highly uncertain and cover a wide range of values. Therefore, a number of sensitivity simulations were performed by changing kinetic rate constants.

4. Results and Discussion

4.1. Base Case

Concentrations of aqueous chemical components through the sandstone-shale transect are presented in Figure 2. To track diffusive transport fronts, a non-reactive tracer concentration of 1 was applied initially to the sandstone grid block. Figure 2a shows tracer concentration distribution at different times. The initial pH in the sandstone is 7.34, and that in shale is 6.69. The imposition of a high CO_2 pressure of 201 bar lowers the pH in the sandstone (Figure 2b), and H^+ diffuses from the sandstone to shale. The minimum pH after 10,000 years is located about 3 m into the shale, which is behind the tracer front due to retardation by chemical reactions. The movement of H^+ is consistent with carbonate behavior (Figure 2c). Early in the simulation, the carbonate concentration and pH in the shale are controlled mainly by kerogen-OS decomposition. Later, they are gradually affected by CO_2 diffusion from the sandstone layer. Total iron (Fe^{+2} + Fe^{+3}) diffuses from the shale to sandstone (Figure 2d) because in the sandstone Fe^{+2} is removed

by precipitation of siderite ($FeCO_3$) and ankerite ($CaMg_{0.3}Fe_{0.7}(CO_3)_2$). Ca^{+2} also diffuses from the shale into the sandstone (Figure 2e) due to ankerite precipitation, its behavior being similar to total iron. A significant Mg^{+2} concentration buildup occurs only after 10,000 yr at a distance range from 2 to 5 m (Figure 2f). Na^+ concentration (Figure 2g) increases up to 10,000 yr due to the dissolution of oligoclase ($CaNa_4Al_6Si_{14}O_{40}$). Simultaneously, Na^+ diffuses from the sandstone to the shale due to the higher abundance of oligoclase in the former (Table 3). Finally Na^+ diffusion reverses direction because oligoclase dissolves completely in both rocks and early precipitated low-albite in the shale starts to dissolve and supply Na^+ to pore fluid. The K^+ concentration (Figure 2h) also increases until 10,000 yr when K-feldspar disappears due to dissolution. Considerably higher K^+ concentration occurs in the sandstone due to the higher K-feldspar abundance. Al^{+3} and SiO_2(aq) concentrations (Figures 2i and 1j) are controlled by the dissolution and precipitation of a number of aluminosilicate minerals. The total sulfur (sulfate and sulfide species) concentration (Figure 2k) is buffered by kerogen-OS dissolution and pyrite precipitation.

We now turn to the dissolution and precipitation of mineral phases along the sandstone-shale transect. The abundances of mineral phases (both primary and secondary) with time are presented in Figure 3. Significant dissolution of calcite occurs in the sandstone due to the lower pH induced by the presence of CO_2 at high pressure (Figure 3a), as can be seen clearly in Figure 6, which gives a time evolution profile in the sandstone. Slight dissolution and precipitation of calcite occurs in the interior of the shale over time. Oligoclase disappears very rapidly between 1,000 and 10,000 yr (Figure 3b) in both sandstone and shale layers. K-feldspar is similarly destroyed just after 10,000 yr in both layers. Chlorite (Figure 3d) dissolution also occurs in both layers to supply Fe^{+2} needed for precipitation of siderite and ankerite. Chlorite disappears in the sandstone just after 1,000 yr. Some chlorite remains in the interior of the shale at 10,000 yr, but no chlorite remains at 100,000 yr. Kaolinite dissolves steadily in both layers (Figure 3e). Na-smectite dissolution occurs mostly in the sandstone and in the shale close to the interface (Figure 3f). Hematite dissolution (Figure 3g) initially occurs in the sandstone to supply Fe^{+2} needed for precipitation of siderite and ankerite, and progressively proceeds into the shale interior over time. This behavior is similar to chlorite dissolution. Kerogen-OS

dissolves steadily and constantly in the shale (Figure 3h). Quartz precipitates in the sandstone but remains essentially at equilibrium in the interior of the shale (Figure 3i). Illite (Figure 3j) precipitates due to dissolution of oligoclase and K-feldspar, particularly in the shale close to the interface. Low-albite precipitation occurs at 10,000 years in both layers but most intensively at a depth of 4 m in the shale (Figure 3k). However, low-albite later disappears to supply Na needed for dawsonite precipitation. Pyrite precipitates steadily in the shale due to the release of sulfide by dissolving kerogen-OS (Figure 3l).

The injected CO_2 is immobilized by precipitation of four carbonate minerals: magnesite ($MgCO_3$), siderite ($FeCO_3$), ankerite ($CaMg_{0.3}Fe_{0.7}(CO_3)_2$), and dawsonite ($NaAlCO_3$ $(OH)_2$). Minor magnesite forms close to the interface in the shale between 1,000 and 10,000 yr (Figure 3m), but later dissolves completely. Therefore, magnesite is not a stable CO_2 trapping mineral in the modeled environment. Siderite precipitates initially only in the sandstone (Figure 3n), but later gradually forms in the shale due to diffusive transport of CO_2 from the sandstone. The detailed temporal evolution of carbonate minerals in the sandstone can be seen in Figure 6. Significant CO_2 is immobilized by precipitation of ankerite and dawsonite (Figures 3o and 3p). After 100,000 years a maximum of approximately 4% and 6% of volume fraction of ankerite and dawsonite are formed in the sandstone. Calcite dissolves under the high CO_2 pressure conditions, and no dolomite ($CaMg(CO_3)_2$) precipitation is observed. The cumulative CO_2 sequestered in carbonate minerals along the sandstone-shale transect is presented in Figure 4. Precipitation of carbonate minerals initially occurs essentially in the sandstone, and later gradually occurs in the shale due to diffusive transport of CO_2 from the sandstone. The precipitation of carbonate minerals results in decrease of porosity (Figures 5 and 8), which is consistent with CO_2 mineral sequestration shown in Figure 4. A slight increase in porosity can be observed in the interior of the shale ($x > 4$ m), indicating leaching chemical constituents from the shale.

After 100,000 years, CO_2 mineral sequestration in the sandstone can reach about 90 kg/m^3 of medium (Figure 7), which is very close to the maximum capacity. The CO_2 trapping capacity depends on the primary mineral composition. Precipitation of siderite and ankerite requires Fe^{+2} supplied mostly by chlorite ($Mg_{2.5}Fe_{2.5}Al_2Si_3O_{10}(OH)_8$) and some by dissolution and reduction of hematite (Fe_2O_3). Precipitation of dawsonite

requires Na^+ provided by oligoclase ($CaNa_4Al_6Si_{14}O_{40}$) dissolution. The initial abundance of chlorite and oligoclase therefore affects the CO_2 mineral trapping capacity. The sequestration time required depends on the kinetics of mineral dissolution and precipitation. In the next section, we discuss sensitivity of CO_2 mineral sequestration to kinetic rate constants.

4.2. Sensitivity

Mineral dissolution and precipitation rates are a product of the kinetic rate constant and reactive surface area (Eq. 1), the magnitudes of which are highly uncertain and cover a wide range of values. Scaling kinetic rate constants (or reactive surface areas) for all minerals by the same factor is equivalent to scaling the time coordinate. These changes result in reciprocal changes in the time scale. Details on scaling kinetic rates by the same factor are given in Xu et al. (2004)

As shown above, significant CO_2 is sequestered by dawsonite precipitation. The overall sequestration time required depends strongly on the kinetics of dawsonite precipitation. Dawsonite reaction kinetics is not well understood. In the previous simulation, we simply set the rate constant equal to that of siderite and ankerite (k_{25} = 1.2589×10^{-9} moles $m^{-2}s^{-1}$ in Table 1). In order to examine the effect of dawsonite precipitation kinetics on sequestration time, two additional simulations were performed by decreasing the rate constant used in the base case by two and three orders of magnitude, respectively. The cumulative CO_2 mineral sequestration after 100,000 years along the sandstone-shale transect obtained by these sensitivity simulations is presented in Figure 9. At the final time (after 100,000 years), total CO_2 sequestered in the sandstone decreases slightly with the rate constant. While, the total amount of CO_2 sequestered in the shale is very close to that in the base case, except that the peak concentration is shifted somewhat towards the sandstone interface. The dawsonite distribution (Figure 10a) after 100,000 years is similar to CO_2 mineral sequestration. The decreases in dawsonite kinetic rate constant results in very slight decreases in ankerite precipitation in the sandstone, and slight increases in the shale (Figure 10b). The detailed temporal evolutions of CO_2 sequestration and carbonate mineral abundance are presented in

Figures 11 and 12, respectively. As expected, the lower rate constant results in less dawsonite precipitation. However, the difference decreases with time when compared to the base case. After 100,000 years, the CO_2 mineral sequestration is only slightly lower than the base case. Thus, a decrease in the dawsonite rate constant by two or three orders of magnitude results in a small decrease in the mineral sequestration. The reason for the small effect is because precipitation of dawsonite requires reactants that are provided by the dissolution of the primary aluminosilicate minerals. For example, Na^+ required by dawsonite precipitation comes from dissolution of oligoclase ($CaNa_4Al_6Si_{14}O_{40}$). In the base case, the dawsonite precipitation rate is limited by the dissolution rate of aluminosilicate minerals even though a higher dawsonite rate constant was used.

4.3. Comparison with field observations

Few mineralogical descriptions of the alteration of sandstone – shale sequences in the presence of high-pressure CO_2 are available in the literature that would allow comparison with the simulation presented in this paper. Those of interest usually reflect past accumulations of CO_2 associated with magmatic or volcanic activity. An example is that by Moore et al. (this issue), who describe the formation of secondary dawsonite and kaolinite in siltstones of the Permian Supai Formation of the Springerville-St. John CO_2 field on the border between Arizona and New Mexico. They observed secondary dawsonite spatially associated with corroded plagioclase and potassium feldspar, which is consistent with our simulations. Furthermore, their determination that kaolinite formed subsequent to dawsonite deposition following a decline in the CO_2 pressure, is also consistent with our finding that kaolinite is unstable during the precipitation of dawsonite. Authigenic illite appears to persist in the presence of dawsonite, which is also consistent with our modeling results. In contrast, the Supai Formation appears to have been more oxidizing, with a limited capacity to provide Fe^{+2} for the stabilization of ankerite.

Another recent paper (Watson et al., 2002) describes mineralogical and groundwater changes caused by magmatic carbon dioxide invading a gas reservoir in a lithic sandstone of the Pretty Hill Formation in the Ladbroke Grove gas field in South Australia. An important feature of this field example is that the mineralogy can be

compared with an adjacent unmodified methane gas reservoir in the same formation. In contrast to those of the Supai Formation of Arizona and New Mexico, the conditions in this high-pressure CO_2 field are such that Fe^{+2} is available for the stabilization of siderite and ankerite. In this respect, the Ladbroke Grove field more closely represents the conditions of our simulation. Observed similarities include the destruction of chlorite in the lithic fragments and net corrosion of the feldspars, a reduction in the concentration of calcite, an increase in the concentration of siderite, a significant increase in the quantity of ankerite and a small increase in the quantity of quartz. However, no dawsonite was reported even though an evaluation of the coexisting groundwater indicates that it should have been supersaturated with respect to this carbonate. A substantial increase in the concentration of kaolinite is observed, which is in conflict with our simulation. The porosity of the Ladbroke Grove reservoir also appears to have increased, whereas our simulation shows a decrease. The differences might be explained by the higher CO_2 pressure (201 vs. approximately 150 bar) and the higher Cl^- and Na^+ concentrations of the simulation.

Other field evidence supports that magmatic CO_2 can also lead to the formation of dawsonite in arenaceous sedimentary formations, notably in the Bowen, Gunnedah and Sydney Basins of New South Wales (Baker et al., 1995), and the Denison Trough of east-central Queensland (Baker, 1991; Baker and Caritat, 1992). Dawsonite and kaolinite in these sedimentary accumulations appear to have been produced at the expense of detrital feldspars, in general agreement with the observations of Moore et al. (this issue). But it should be noted that feldspar destruction is incomplete, and on occasion, dawsonite is found in juxtaposition with unaltered feldspar (Loughnan and Goldbery, 1972). The field evidence is therefore suggestive of slow feldspar corrosion rates if not the eventual stabilization of feldspars. In these sedimentary formations, the occurrence of dawsonite is unrelated to the preceding precipitation or dissolution of diagenetic calcite, siderite and ankerite, which is attributed to early diagenesis and subsequent organic maturation (Baker, 1991).

Carbonate paragenesis in sedimentary formations invaded by magmatic CO_2 can vary in degree and complexity. The mineralogy, burial history, diagenesis, organic maturation, temperature and connate water salinity all play a role in addition to the timing

and extent of magmatic CO_2 involvement. Thus it is hardly surprising that agreement between the present simulations and field observations is not perfect in all respects.

5. Summary and Conclusions

A reactive geochemical transport model for a sandstone-shale system under high CO_2 pressure conditions has been developed. The model has been used to analyze mass transfer of aqueous chemical components, the alteration pattern of minerals, sequestration of CO_2 by secondary carbonates, and changes of porosity for a Gulf Coast aquifer.

CO_2 diffuses from the sandstone (where CO_2 is initially injected), lowering pH. Fe^{+2} from chlorite dissolution and Ca^{+2} from oligoclase dissolution diffuses from the shale to sandstone to supply reactants needed for precipitation of siderite and ankerite. but later reverses direction. Na^+ in contrast to Ca^{+2}, initially diffuses from the shale to sandstone, but later reverses direction. Total iron behaves similarly to Ca^{+2}, due to significant precipitation of ankerite in the sandstone. Initially, Na^+ diffuses from the sandstone to shale due to higher dissolution rate of oligoclase in the sandstone than in the shale. Finally Na^+ reverses diffusion direction from the shale to sandstone because oligoclase dissolved completely in both layers and early precipitated low-albite in the shale starts to dissolve to supply Na^+ for dawsonite precipitation

Most CO_2 sequestration occurs in the sandstone. The major CO_2 trapping minerals are dawsonite and ankerite. The CO_2 mineral-trapping capacity after 100,000 years reaches 90 kg/m^3 of medium. Precipitation of secondary carbonates results in decreased porosity. Leaching of chemical constituents from the interior of the shale causes slightly increased porosity. The CO_2 trapping capacity depends on its primary mineral composition. Precipitation of siderite and ankerite requires Fe^{+2} supplied mainly by chlorite and by some hematite dissolution. Precipitation of dawsonite requires Na^+ provided by oligoclase dissolution. Therefore, the initial abundance of chlorite and oligoclase affects CO_2 mineral trapping capacity.

The sequestration time required depends on the rates of mineral dissolution and precipitation, which are products of the kinetic rate constant and reactive surface area.

Scaling kinetic rates for all minerals by the same factor is equivalent to scaling the time coordinate. Such changes result in reciprocal changes to the time scale. Significant CO_2 is sequestered by dawsonite precipitation. However, dawsonite reaction kinetics are not well understood. The sensitivity regarding dawsonite precipitation rate was examined. Decreases in the rate constant by two and three orders of magnitude result in small decreases in the CO_2 sequestration, because precipitation of dawsonite requires reactants whose availability is controlled by the dissolution of aluminosilicate minerals. In the base case, the dawsonite precipitation rate is limited by the dissolution rate of aluminosilicate minerals even though a higher dawsonite rate constant was used. The overall rate is the lowest value among the participating minerals.

Limited information currently available describing the mineralogy of natural high-pressure CO_2 gas reservoirs is also generally consistent with our simulation.

The model investigated here assumes perfect mixing throughout the sand layer. Future work should examine the effect of regional groundwater flow, including the possibility that groundwater flow in the sandstone is sufficiently slow, so that chemical gradients may develop within the sandstone as a function of distance from the interface with the shale.

The range of problems concerning the interaction of water-CO_2-rock is very broad. The present simulation results are specific to the conditions and parameters considered. The "numerical experiments" give a detailed understanding of the dynamic evolution of a sandstone-shale geochemical system.

Acknowledgement. We thank Curtis Oldenburg and Guoxiang Zhang for the internal reviews of the manuscript. We acknowledge Jacques Schott, Sigurdur Reynir Gislason, and two anonymous reviewers for their detailed helpful suggestions and comments during the review process that significantly improved the quality of the paper. This work was supported by the Director, Office of Science, Office of Basic Energy Sciences, of the U.S. Department of Energy, under Contract No. DE-AC03-76SF00098 with Lawrence Berkeley National Laboratory.

References

Ague, J.J., Brimhall, G.H., 1989. Geochemical modeling of steady state and chemical reaction during supergene enrichment of porphyry copper deposits. Economic Geology 84, 506-528.

Arnorsson, S., Stefansson, A., 1999. Assessment of feldspar solubility constants in water in the range 0^{o} to 350^{o}C at vapor saturation pressures. Am. J. Sci. 299, 173-209.

Bachu, S., Gunter, W.D., Perkins, E.H., 1994. Aquifer disposal of CO_2: hydrodynamic and mineral trapping. Energy Convers. Mgmt. 35, 269-279.

Baroody, E.E., Carpenter, G.A., 1972. Heats of formation of propellant compounds (U), Rpt Naval Ordnance Systems Command task No. 331-003/067-1UR2402-001 for Naval Ordnance station, Indian Head, MD. 1-9 p.

Blum, A.E., Stillings, L.L., 1995. Feldspar dissolution kinetics, Chapter 7 of chemical weathering rates of silicate minerals, White, A.F., Brantley, S.L. (eds.), Mineral Society of America 31, 291–351, Washington D. C.

Boram, L.H., Higgins, S.R., Knauss, K.G., Eggleston, C.M., 2002. Plagioclase dissolution and carbonate growth related to co2 sequestration in deep aquifers: EQ3/6 modeling and laboratory experiments. 2002 Geological Society of America Annual Meeting, Session 135 (4), October 27-30, Denver, Colorado.

Capuano, R.M., 1993. Evidence of fluid flow in microfractures in geopressured shales. AAPG Bulletin 77(8), 1303-1314.

Carlson, H.G., Westrum, E.F., Jr., 1971. Methanol: heat capacity, enthalpies of transition and melting, and thermodynamic properties from 5-300 K. J. Chem. Phys. 54, 1464-1471.

Chai, L., Navrotsky, A., 1996. Synthesis, characterization, and energetics of solid solution along the dolomite-ankerite join, and implications for the stability of ordered CaFe(CO3)2. American Mineralogist 81, 1141-1147.

Chou L., Garrels R.M., and Wollast R., 1989. Comparative study of the kinetics and mechanisms of dissolution of carbonate minerals. *Chem. Geol.* 78, 269-282.

Corey, A.T., 1954, The interrelation between gas and oil relative permeabilities, Producers Monthly, 38 – 41.

Ferrante, M.J., Stuve, J.M., Richardson, D.W., 1976. Thermodynamic data for synthetic dawsonite. U. S. Bureau of Mines Report of Investigations No. 8129, 13 pp.

Folk, R.L., 1968. Petrology of Sedimentary Rocks. Hemphill Publishing Company, Austin, Texas, 182 pp.

Gautelier M., Oelkers E.H., and Schott J., 1999. An experimental study of dolomite dissolution rates as a function of pH from -0.5 to 5 and temperature from 25 to 80°C. *Chem. Geol.* 157, 13-26.

Giammar, D.E., Bruant, R.G., Peters, C.A., 2002. Silicate weathering at pressure, temperature, and aqueous carbon dioxide conditions relevant to geologic carbon sequestration. 2002 Geological Society of America Annual Meeting, Session 135 (6), October 27-30, Denver, Colorado.

Good, W.D., Lacina, J.L., McCullough, J.P., 1961. Methanethiol and carbon disulfide: Heats of combustion and formation by rotating-bomb calorimetry. J. Phys. Chem. 65, 2229-2231.

Goodman, A.L., Soong, Y., Strazisar, B., Hedges, S.W., Jones, J.R., Harrison, D.K., Zhu, C., 2002. Carbon dioxide sequestration with brines, 2002 Geological Society of America Annual Meeting, Session 135 (8), October 27-30, Denver, Colorado.

Gunter W.D., Perkins, E.H., McCann, T.J., 1993. Aquifer disposal of CO_2-rich gases: Reaction design for added capacity. Energy Convers. Mgmt. 34, 941-948.

Gunter W.D., Bachu, S., Law, D.H.S., Marwaha, V., Drysdale, D.L., MacDonald, D.E., McCann, T.J., 1996. Technical and economic feasibility of CO_2 disposal in aquifers within the Alberta Sedimentary Basin, Canada. Energy Convers. Mgmt. 37, 1135-1142.

Gunter W.D., Wiwchar, B., Perkins, E.H., 1997. Aquifer disposal of CO_2-rich greenhouse gases: extension of the time scale of experiment for CO_2-sequestering reactions by geochemical modeling. Mineral. and Petrol. 59, 121-140.

Hedges, S.W., Zhu, C., Dubose, S.B., 2002. Experimental investigation of gas/water/rock interactions relevant to geological CO2 sequestration. 2002 Geological Society of America Annual Meeting, Session 135 (9), October 27-30, Denver, Colorado.

Helgeson, H.C., Kirkham, D.H., Flowers, G.C., 1981. Theoretical prediction of the thermodynamic behavior of aqueous electrolytes at high pressures and temperatures: IV. Calculation of activity coefficients, osmotic coefficients, and apparent molal and standard and relative partial molal properties to 600 C and 5 kb. Am. J. Sci. 281, 1249–1516.

Helgeson, H.C., Delany, J.M., Nesbit, H.W., Bird, D.K., 1978. Summary and critique of the thermodynamic properties of minerals, Am. J. Sci. 278A. 229 pp.

Helgeson, H.C., Owens, C.E., Knox, A.M., Richard, L., 1998. Calculation of the standard molal thermodynamic properties of crystalline, liquid, and gas organic molecules at high temperatures and pressures. Geochim et Cosmochim Acta, 62(6), 985-1081.

Hold, M., Brussee, N.J., Schouten, S., and Sinninghe Damste, J.S., 1998. Changes in the molecular structure of a Type II-S kerogen (Monterey Formation, U.S.A.) during sequential chemical degradation. Organic Geochemistry 29(5-7), 1403-1417.

Holland, T.J.B., Powell, R., 1998. In internally consistent thermodynamic data set for phases of petrological interest. Journal of Metamorphic Geology 16(3), 309-343.

Holloway, S., 1997. An overview of the underground disposal of carbon dioxide. Energy Convers. Mgmt. 38, 193-198.

Horita, J., 2002. Profilometer-based study of nanometer- to millimeter-scale growth kinetics of calcite from CO2-rich fluids. 2002 Geological Society of America Annual Meeting, Session 135 (12), October 27-30, Denver, Colorado.

Hovorka, S. D., Knox, P. R., Holtz, M. H., Yeh, J. S., Fouad, K., Sakurai, S., 2002. Sequestration pilot site in the Texas Gulf coast, USA. 2002 Geological Society of America Annual Meeting, Session 135 (10), October 27-30, Denver, Colorado.

Howard, J.J., 1991. Porosimetry measurement of shale fabric and its relationship to illite/smectite diagenesis. Clays and Clay Minerals, 39(4), 355-361.

Hower, J., Eslinger, E.V., Hower, M.E., Perry, E.A., 1976. Mechanism of burial metamorphism of argillaceous sediment, I: Mineralogical and chemical evidence. GSA Bulletin 87, 725-737.

Johnson, J.W., Oelkers, E.H., Helgeson, H.C., 1992. SUPCRT92: A software package for calculating the standard molal thermodynamic properties of minerals, gases,

aqueous species, and reactions from 1 to 5000 bars and 0 to 1000 degrees C. Computers and Geosciences 18, 899–947.

Johnson. J.W., Nitao, J.J., Steefel, C.I., Knaus, K.G., 2001. Reactive transport modeling of geologic CO_2 sequestration in saline aquifers: The influence of intra-aquifer shales and the relative effectiveness of structural, solubility, and mineral trapping during prograde and retrograde sequestration, In proceedings: First National Conference on Carbon Sequestration. Washington, DC.

Jones, J. R. M., Soong, Y., Harrison, D. K., Lasota, K. A., White, C. M., 2002. Mineral trapping potential of brine aquifers to sequester anthropogenic CO2, 2002 Geological Society of America Annual Meeting, Session 135 (7), October 27-30, Denver, Colorado.

Kaszuba, J. P., Janecky, D. R., Snow, M., 2002. Experimental evaluation of mixed fluid reactions between supercritical carbon dioxide and a nacl brine: relevance to geologic aquifer carbon sequestration. 2002 Geological Society of America Annual Meeting, Session 135 (3), October 27-30, Denver, Colorado.

Knauss, K. G., Steefel, C. I., Johnson, J. W., Boram, L. H., 2002. Impact of CO2, contaminant gas, aqueous fluid, and reservoir rock interactions on the geologic sequestration of CO2, Knauss. 2002 Geological Society of America Annual Meeting, Session 135 (13), October 27-30, Denver, Colorado.

Korbol, R., Kaddour, A., 1995. Sleipner vest CO_2 disposal - injection of removed CO_2 into the Utsira Formation. Energy Convers. Mgmt. 36 (6-9), 509-512.

Kreitler, C.W., Richter, B.C., 1986. Hydrochemical characterization of saline aquifers of the Texas Gulf Coast used for the disposal of industrial waste. Report to the US Environmental protection Agency under Cooperative agreement No. CR821786-01-0. University of Texas at Austin, Bureau of Economic Geology.

Kulik, D.A., Aja, S.U., 1997 (July 20-24). Hydrothermal stability of illite: implications of empirical correlations and Gibbs Energy minimization. Proceedings on the Fifth International Symposium on Hydrothermal Reactions, Gatlinburg, Tennessee, 228-292.

Land, L.S., 1984. Frio sandstone diagenesis, Texas Gulf Coast: A regional isotopic study. In Clastic Diagenesis, (David A. McDonald and Ronald C. Surdam, Eds.) AAG Memoir 37, Part 1. Concepts and Principles, 47-62.

Land, L.S., Mack, L.E., Milliken, K.L., Lynch, F.L., 1997. Burial diagenesis of argillaceous sediment, south Texas Gulf of Mexico sedimentary basin: A reexamination. GSA Bulletin 109(1), 2-15.

Lasaga, A.C., 1984. Chemical kinetics of water-rock interactions, J. Geophys. Res. 89, 4009-4025.

Lasaga, A.C., and Luttge, A., 2001. Variation of crystal dissolution rate based on a dissolution stepwave model. Science 291, 2400-2404.

Law, D.H.S., Bachu, S., 1996. Hydrogeological and numerical analysis of CO_2 disposal in deep aquifers in the Alberta Sedimentary Basin. Energy Convers. Mgmt. 37(6-8), 1167 - 1174.

Lohuis, J.A.O., 1993. Carbon dioxide disposal and sustainable development in The Netherlands, Energy Convers. Mgmt. 34(9-11), 815-821.

Loucks, R.G., Dodge, M.M., and Galloway, W.E., 1984. Regional controls on diagenesis and reservoir quality in Lower Tertiary sandstones along the Texas Gulf Coast. In Clastic Diagenesis, (David A. McDonald and Ronald C. Surdam, Eds.) AAPG Memoir 37, Part 1. Concepts and Principles, p.15-45.

Lynch, F. L., 1997, Frio shale mineralogy and the stoichiometry of the smectite-to-illite reaction: the most important Reaction in clastic sedimentary diagenesis. Clays and Clay Minerals 45(5), 618-631.

Malmstrom M., Banwart S., Lewenhagen J., Duro L., and Bruno J., 1996. The dissolution of biotite and chlorite at 25ºC in the near-neutral pH region. *Contaminant Hydrology,* 21, 201-213.

Matter, J. M., Takahashi, T., Goldberg, D., Morin, R. H., Stute, M., 2002. Secure, long-term geological carbon sequestration in mafic rocks: Results from field and laboratory experiments, 2002 Geological Society of America Annual Meeting, Session 135 (5), October 27-30, Denver, Colorado.

McPherson, B.J.O.L., Lichtner, P.C., 2001. CO_2 sequestration in deep aquifers, In proceedings: First National Conference on Carbon Sequestration. Washington, DC.

Moore, J., Adams, M., Allis, R., Lutz, S., Rauzi, S., 2004. Mineralogical and geochemical consequences of the long term presence of CO_2 in natural reservoirs: An example from the Springerville-St. Johns field, Arizona and New Mexico, USA. Chemical Geology, This issue.

Nagy, K.L., 1995. Dissolution and precipitation kinetics of sheet silicates, Chemical Weathering Rates of Silicate Minerals 31, 291–351.

Narasimhan, T.N., Witherspoon, P.A., 1976. An integrated finite difference method for analyzing fluid flow in porous media, Water Resour. Res. 12, 57–64.

Nordstrom, D.K., 1984. Partial compilation and revision of basic data in the Wateq programs. U.S. geol. Surv. WRI Rept. #84-4186, 40 pp.

Nordstrom, D.K., Muñoz, J.L., 1986. Geochemical Thermodynamics, The Benjamin/Cummings Pub. Co., Menlo Park, California, 477 pp.

Oelkers, E. H., Pokrovsky, O., Schott, J., 2002. An experimental study of magnesite dissolution and precipitation rates, 2002 Geological Society of America, Session 135 (1), October 27-30, Denver, Colorado.

Ortoleva, P.J., Dove, P., Richter, F., 1998 (May 10-12). Geochemical perspectives on CO_2 sequestration, Manuscript prepared for U. S. Department of Energy Workshop on "Terrestrial Sequestration of CO_2 - An Assessment of Research Needs," Gaithersburg, MD.

Palandri, J. L., Kharaka, Y. K., 2002. Adding kinetics to equilibrium-based geochemical modeling of CO2 sequestration. 2002 Geological Society of America Annual Meeting, Session 174 (5), October 27-30, Denver, Colorado.

Parker, V.B., Khodakovskii, I.L., 1995. Thermodynamic properties of the aqueous ions (2+ and 3+) of iron and key compounds of iron. J. Phys. Chem. Ref. Data 24(5), 1699-1745.

Parkhurst, D.L., Thorstenson, D.C., Plummer, L.N., 1980. PHREEQE: A computer program for geochemical calculations: US Geological Survey, Water Resources Investigation 80-96, 174 pp.

Pearce, J.M., Holloway, S., Wacker, H., Nelis, M.K., Rochelle, C., Bateman, K., 1996. Natural occurrences as analogues for the geological disposal of carbon dioxide. Energy Convers. Mgmt. 37 (6-8), 1123-1128.

Perkins, E.H., Gunter, W.D., 1995. A users manual for PATHARC.94: a reaction path-mass transfer program, Alberta Research Council Report ENVTR 95-11, 179 pp., Canada.

Perkins, E.H., Gunter, W.D., Hutcheon, I., Shevalier, M., Durocher, K., Emberley, S., 2002. Geochemical modelling and monitoring of CO2 storage at the Weyburn site, Saskatchewan, Canada, 2002 Geological Society of America Annual Meeting, Session 174 (11), October 27-30, Denver, Colorado.

Preis, W., Gamsjager, H., 2002. Critical evaluation of solubility data: enthalpy of formation of siderite. Phys. Chem. Chem. Phys. 4, 4014-4019.

Pruess, K., Oldenburg, C., Moridis, G., 1999. TOUGH2 user's guide, Version 2.0. Lawrence Berkeley Laboratory Report LBL-43134, Berkeley, California.

Pruess, K., Xu, T., Apps, J., García, J., 2003. Numerical modeling of aquifer disposal of CO2. SPE (Society of Petroleum Engineers) Journal, March (2003), p. 49-59.

Reardon, E.J., Beckie, R.D., 1987. Modelling chemical equilibria of acid mine drainage: The FeSO4-H2SO4-H2O system. Geochim. et Cosmochim. Acta, 51, 2355-2368.

Reed, M.H., 1982. Calculation of multicomponent chemical equilibria and reaction processes in systems involving minerals, gases and aqueous phase. Geochim. et Cosmochim. Acta 46, 513-528.

Richard, L., Helgeson, H.C., 1998. Calculation of the thermodynamic properties at elevated temperatures and pressures of saturated and aromatic high molecular weight and liquid hydrocarbons in kerogen, bitumen, petroleum and other organic matter of biogeochemical interest. Geochim et Cosmochim Acta, 62(23-24), 3591-3636.

Rimstidt, J.D., 1997. Quartz solubility at low temperatures. Geochim. et Cosmochim. Acta 61, 2553-2558.

Robie, R.A., Hemingway, B.S., 1995. Thermodynamic properties of minerals and related substances at 298.15 K and 1 bar (10^5 Pascals) pressure and at higher temperatures. U.S. Geol. Surv. Bull. 2131, 461 p.

Rock, P.A., Mandell, G.K., Casey, W.H., Walling, E.M., 2001. Gibbs energy of formation of dolomite from electrochemical cell measurements and theoretical calculations. Am. J. Sci. 301, 103-111.

Rochelle, C.A., Bateman, K., Pearce, J.M., 1996. Fluid-rock interactions resulting from the underground disposal of carbon dioxide, In Bottrell, S. H. (ed.), Proc., 4th lnt. Symp. Geochem, Earth's Surf.. University of Leeds, Dep. of Earth Sciences, Leeds, UK., 448-452.

Rosenbauer, R. J., Koksalan, T., 2002. Experimental determination of the solubility of CO2 in electrolytes: Application to CO2 sequestration in deep-saline aquifers. 2002 Geological Society of America Annual Meeting, Session 135 (2), October 27-30, Denver, Colorado.

Russell, H., Jr., Osborne, D.W., Yost, D.M., 1942. The heat capacity, entropy, heats of fusion, transition, and vaporization and vapor pressures of methyl mercaptan. J. Am. Chem. Soc. 64, 165-169.

Shock, E.L., Sassani, D.C., Willis, M., Sverjensky, D.A., 1997. Inorganic species in geologic fluids, Correlations among standard molal thermodynamic properties of aqueous ions and hydroxide complexes. Geochim. et Cosmochim. Acta 61, 907-950.

Solano-Acosta, W., Rupp, J., Zuppann, C.W., 2002. Estimating the CO2 sequestration capacity of deep saline aquifers in southwestern Indiana. 2002 Geological Society of America Annual Meeting, Session 174 (4), October 27-30, Denver, Colorado.

Sonnenthal, E.L., Spycher, N., 2001. Drift-Scale coupled processes (DST and THC seepage) models. AMR N0120/U0110 Rev.01, Yucca Mountain Project, Lawrence Berkeley National Laboratory, Berkeley, California.

Steefel, C.I., van Cappellen, P., 1990. A new kinetic approach to modeling water-rock interaction: The role of nucleation, precursors and Ostwald ripening. Geochim. Cosmochim. Acta 54, 2657-2677.

Steefel, C.I., Lasaga, A.C., 1994. A coupled model for transport of multiple chemical species and kinetic precipitation/dissolution reactions with applications to reactive flow in single phase hydrothermal system. Am. J. Sci. 294, 529-592.

Steefel C. I., 2001. CRUNCH, Lawrence Livermore National Laboratory, pp. 76.

Strazisar, B. R., Zhu, C., 2002. One-dimensional reactive transport model for geological carbon sequestration, 2002 Geological Society of America Annual Meeting, Session 174 (6), October 27-30, Denver, Colorado.

Tester, J.W., Worley, G.W., Robinson, B.A., Grigsby, C.O., Feerer, J.L., 1994. Correlating quartz dissolution kinetics in pure water from 25° to 625 °C., Geochim. et Cosmochim. Acta 58, 2407–2420.

Tissot, B.P., Welte, D.H., 1978. Petroleum formation and occurrence: A new approach to oil and gas exploration. Springer Verlag, New York, 538 pp.

van Genuchten, M. Th., 1980, A Closed-form equation for predicting the hydraulic conductivity of unsaturated soils, Soil Sci. Soc. Am. J. 44, 892 – 898.

Verma, A., Pruess, K., 1988. Thermohydrological conditions and silica redistribution near high-level nuclear wastes emplaced in saturated geological formations. J. Geophys. Res., 93, 1159-1173.

Watson, M.N., Zwingmann, N., Lemon, N.M., 2002 (October 1-4). The Ladbroke Grove-Katnook carbon dioxide natural laboratory: A recent CO_2 accumulation in a lithic sandstone reservoir. Extended Abstract E1-5, Siixth International Conference on Greenhouse Gas Control Technologies (GHCT-6), Kyoto, Japan, 6 p.

White, S.P., Weir, G. J., Kissling, W.M., 2001(May 14-17). Numerical simulation of CO_2 sequestration in natural CO_2 reservoirs on the Colorado Plateau. In Proceedings of First National Conference on Carbon Sequestration, Washington, DC.

Wolery, T.J., 1992. EQ3/6: Software package for geochemical modeling of aqueous systems: Package overview and installation guide (version 7.0). Lawrence Livermore National Laboratory Report UCRL-MA-110662 PT I, Livermore, California.

Xu, T., Pruess, K., 1998. Coupled modeling of non-isothermal multiphase flow, solute transport and reactive chemistry in porous and fractured media: 1. Model development and validation. Lawrence Berkeley National Laboratory Report LBNL-42050, Berkeley, California, 38 pp.

Xu, T., Apps, J., Pruess, K., 2000. Analysis of mineral trapping for CO_2 disposal in deep aquifers, Lawrence Berkeley National Laboratory Report LBNL-46992, Berkeley, California, 106 pp.

Xu, T., Pruess, K., 2001, Modeling multiphase non-isothermal fluid flow and reactive geochemical transport in variably saturated fractured rocks: 1. Methodology, Am. J. Sci., 301, 16-33.

Xu, T, Apps, J.A., Pruess, K., 2003. Reactive geochemical transport simulation to study mineral trapping for CO_2 disposal in deep arenaceous formations, Journal of Geophysical Research 108(B2).

Xu, T, Apps, J.A., Pruess, K., 2004. Numerical simulation to study mineral trapping for CO_2 disposal in deep aquifers, Applied Geochemistry, 19, 917-936.

Yeh, G.T., Tripathi, V.S., 1991. A model for simulating transport of reactive multispecies components: model development and demonstration. Water Resour. Res. 27, 3075-3094.

Zotov, A., Mukhamet-Galeev, A., Schott, J., 1998. An experimental study of kaolinite and dickite relative stability at 150-300 °C and the thermodynamic properties of dickite. American Mineralogist (1998), 83(5-6), 516-524.

Table 1. List of kinetic rate parameters used in Eqs. (1) and (2) for minerals considered in the present simulations (The rate constant k_{25} is for far from equilibrium conditions).

Mineral	k_{25} (moles $m^{-2}s^{-1}$)	E_a (KJ/mol)	n	Reference	Surface area (cm^2/g)
calcite	Equilibrium				
quartz	$1.26x10^{-14}$	87.50	0	Tester et al. (1994)	9.8
K-feldspar	$1.00x10^{-12}$	57.78	0	Blum and Stillings (1995)	9.8
	$3.55x10^{-10}$	51.83	0.4	Blum and Stillings (1995)	9.8
kaolinite	$1.00x10^{-13}$	62.76	0	Nagy (1995)	151.6
	$4.37x10^{-12}$	62.76	0.17	Nagy (1995)	151.6
magnesite	$4.47x10^{-10}$	62.76	0	Chou et al. (1989)	9.8
	$4.37x10^{-5}$	18.98	1.0	Chou et al. (1989)	9.8
siderite	$1.26x10^{-9}$	62.76	0	Steefel (2001)	9.8
	$1.02x10^{-3}$	20.90	0.9	Gautelier et al. (1999)	9.8
dolomite	$1.26x10^{-9}$	62.76	0	Set to siderite	9.8
	$1.02x10^{-3}$	20.90	0.9	Set to siderite	9.8
ankerite	$1.26x10^{-9}$	62.76	0	Set to siderite	9.8
	$1.02x10^{-3}$	20.90	0.9	Set to siderite	9.8
dawsonite	$1.26x10^{-9}$	62.76	0	Set to siderite	9.8
	$1.02x10^{-3}$	20.90	0.9	Set to siderite	9.8
kerogen-OS	$1.00x10^{-13}$	0.0	0.0	Assumed	10
oligoclase	$1.00x10^{-12}$	57.78	0	Set to K-feldspar	10
	$3.55x10^{-10}$	51.83	0.4	Set to K-feldspar	10
albite-low	$1.00x10^{-12}$	67.83	0	Blum and Stillings (1995)	9.8
	$2.04x10^{-10}$	59.77	0.5	Blum and Stillings (1995)	98
Na-smectite	$1.00x10^{-13}$	62.76	0	Set to kaolinite	151.6
	$4.37x10^{-12}$	62.76	0.17	Set to kaolinite	151.6
Ca-smectite	$1.00x10^{-13}$	62.76	0	Set to kaolinite	151.6
	$4.37x10^{-12}$	62.76	0.17	Set to kaolinite	151.6
illite	$1.00x10^{-13}$	62.76	0	Set to kaolinite	151.6
	$4.37x10^{-12}$	62.76	0.17	Set to kaolinite	151.6
pyrite	$4.00x10^{-11}$	62.76	0	Ague and Brimhall (1989)	12.9
hematite	$4.00x10^{-11}$	62.76	0	Set to pyrite	12.9
chlorite	$2.51x10^{-12}$	62.76	0	Malmstrom et al. (1996)	9.8

Table 2. Hydrogeologic parameters for sandstone and shale layers.

Parameters	Sandstone	Shale
Permeability (m^2) Porosity Tortuosity Compressibility (Pa^{-1}) Diffusivity (m^2/s)	10^{-13} 0.3 0.3 $1x10^{-8}$ $1x10^{-9}$	10^{-18} 0.1 0.1 $1x10^{-8}$ $1x10^{-9}$
Relative permeability		
Liquid (van Genuchten, 1980): $k_{rl} = \sqrt{S^*}\left\{1-\left(1-\left[S^*\right]^{1/m}\right)^m\right\}^2$ S_{lr} : irreducible water saturation m: exponent	$S^* = (S_l - S_{lr})/(1-S_{lr})$ $S_{lr} = 0.00$ $m = 0.457$	$S_{lr} = 0.00$ $m = 0.457$
Gas (Corey, 1954): $k_{rg} = (1-\hat{S})^2(1-\hat{S}^2)$ S_{gr} : irreducible gas saturation	$\hat{S} = \frac{(S_l - S_{lr})}{(S_l - S_{lr} - S_{gr})}$ $S_{gr} = 0.05$	$S_{gr} = 0.05$
Capillary pressure		
van Genuchten (1980) $P_{cap} = -P_0\left(\left[S^*\right]^{-1/m} - 1\right)^{1-m}$ S_{lr} : irreducible water saturation m: exponent P_0 : strength coefficient	$S^* = (S_l - S_{lr})/(1-S_{lr})$ $S_{lr} = 0.00$ $m = 0.457$ $P_0 = 19.61\,kPa$	$S_{lr} = 0.00$ $m = 0.457$ $P_0 = 6.2\,MPa$

Table 3. List of initial mineral volume fractions and secondary mineral phases for sandstone and shale layers (dolomite and Ca-smectite were included in the list of possible secondary mineral phases the simulations but they were not formed).

Mineral	Chemical composition	Vol.% of solid rock		Vol.% of medium	
		Sandstone	Shale	Sandstone	Shale
***Primary*:**					
quartz	SiO_2	58	19.22	40.6	17.3
kaolinite	$Al_2Si_2O_5(OH)_4$	2.02	4.37	1.41	3.95
calcite	$CaCO_3$	1.93	10.9	1.35	9.81
illite	$K_{0.6}Mg_{0.25}Al_{1.8}(Al_{0.5}Si_{3.5}O_{10})(OH)_2$	1.0	28.14	0.7	25.33
kerogen-OS	$C_{64}H_{102}O_{40}S_{10}$	0.0	2.0	0.0	1.8
oligoclase	$CaNa_4Al_6Si_{14}O_{40}$	19.8	5.28	13.86	4.75
K-feldspar	$KAlSi_3O_8$	8.2	4.74	5.74	4.27
Na-smectite	$Na_{0.290}Mg_{0.26}Al_{1.77}Si_{3.97}O_{10}(OH)_2$	4	23.0	2.8	20.7
chlorite	$Mg_{2.5}\ Fe_{2.5}Al_2Si_3O_{10}(OH)_8$	4.55	2.35	3.19	2.12
hematite	Fe_2O_3	0.5	0.0	0.35	0.0
porosity	----	----	----	30	10
***Secondary*:**					
anhydrite	$CaSO_4$				
magnesite	$MgCO_3$				
low-albite	$NaAlSi_3O_8$				
siderite	$FeCO_3$				
pyrite	FeS_2				
ankerite	$CaMg_{0.3}Fe_{0.7}(CO_3)_2$				
dawsonite	$NaAlCO_3\ (OH)_2$				
alunite	$KAl_3\ (OH)_6(SO_4)_2$				

Table 4. Initial total dissolved component concentrations (mol/kg H_2O) for reactive transport simulations in the sandstone-shale system. (Iron is the sum of Fe^{+2} , Fe^{+3} and their related complexes. Carbon is the sum of CO_2(aq), CH_4(aq), and their related species such as HCO_3^- and acetic acid(aq). Sulfur is the sum of sulfate and sulfide species)

Component	Sandstone	Shale
Ca^{+2}	3.23×10^{-3}	6.57×10^{-2}
Mg^{+2}	1.53×10^{-7}	6.47×10^{-7}
Na^{+}	0.99	0.83
K^{+}	7.52×10^{-3}	5.6×10^{-5}
Iron	2.42×10^{-5}	4.92×10^{-4}
SiO_2(aq)	7.26×10^{-4}	5.89×10^{-4}
Carbon	4.32×10^{-2}	0.92
Sulfur	1.32×10^{-9}	9.72×10^{-7}
Al^{+3}	2.66×10^{-8}	5.41×10^{-8}
Cl^{-}	1.0	1.0
pH	7.34	6.69
Temperature	75°C	75°C

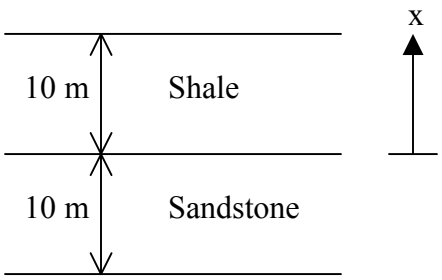

Figure 1. Simplified conceptual model for a sandstone-shale system.

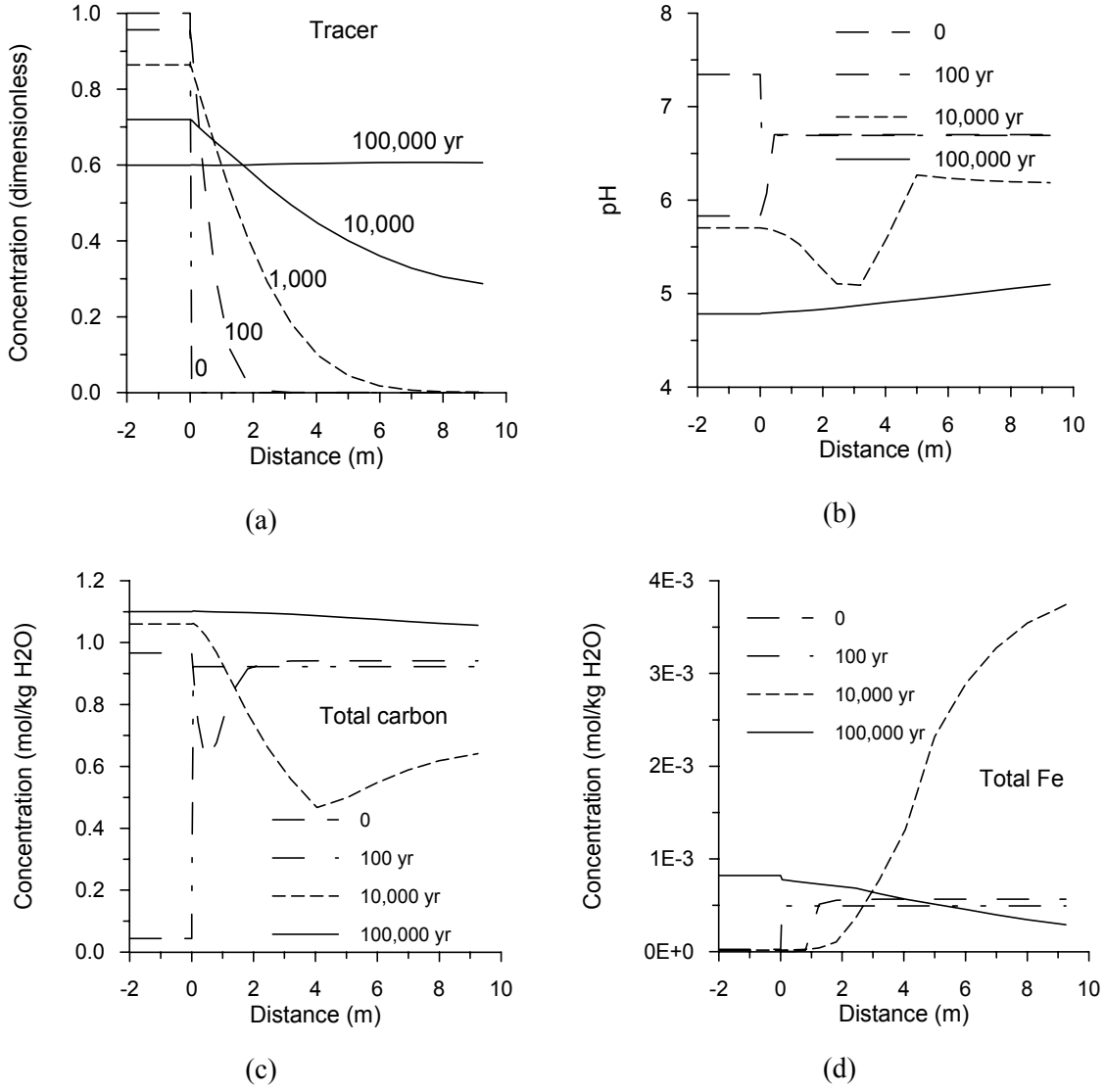

Figure 2. Concentrations of aqueous chemical components and pH along the sandstone-shale transect (x = 0 is the interface between sandstone and shale layers. Only two meters of the sandstone layer is shown in the figures where x < 0). (a) A non-reactive tracer of unit concentration was applied in the sandstone grid block to track diffusive transport fronts; (b) The initial pH in sandstone is 7.34, and that in shale is 6.69. The imposition of the high CO_2 pressure decreases pH; (c) At initial times, the carbonate concentration and pH in the shale are mainly controlled by kerogen-OS decomposition, and later they are gradually affected by CO_2 diffusion from the sandstone layer; (d) Total iron diffuses from the shale to sandstone, because in the sandstone Fe is consumed by precipitation of siderite ($FeCO_3$) and ankerite ($CaMg_{0.3}Fe_{0.7}(CO_3)_2$).

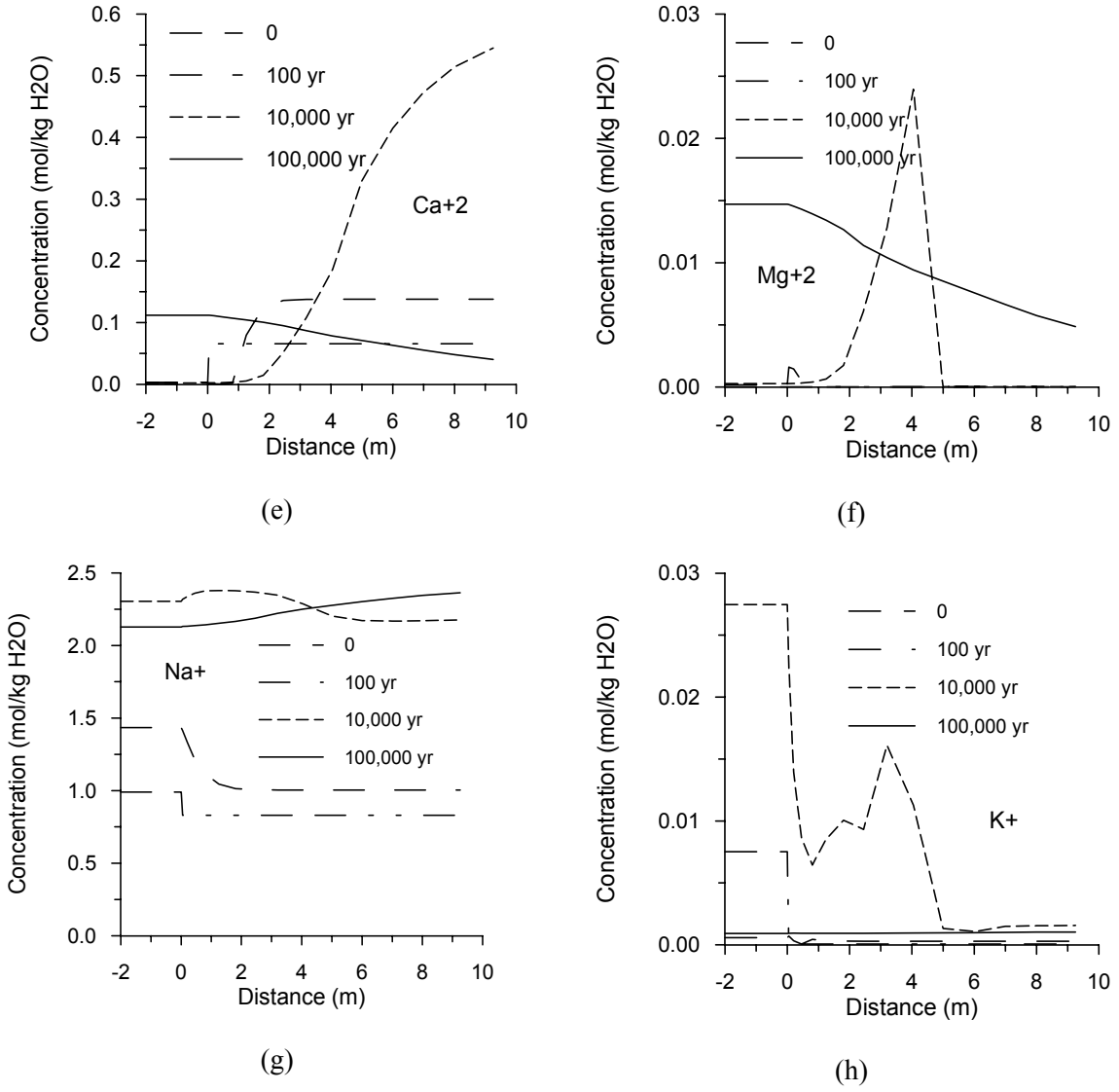

Figure 2. (Continued). (e) Ca^{+2} diffuses from the shale into the sandstone due to ankerite precipitation; (f) Significant Mg^{+2} concentration occurs only after 10,000 yr at a distance into the shale from 2 to 5 m; (g) Na^{+} concentration increases until 10,000 yr due to dissolution of oligoclase ($CaNa_4Al_6Si_{14}O_{40}$), while consequently, Na^{+} diffuses from the sandstone to the shale due to a higher abundance of oligoclase in the sandstone than in the shale. Finally Na^{+} diffusion reverses direction from the shale to the sandstone, because oligoclase has dissolved completely in both layers and early precipitated low-albite in the shale starts to dissolve to supply Na^{+}; (h) K^{+} concentration increases until 10,000 yr when K-feldspar disappears due to dissolution. A considerably higher K^{+} concentration occurs in the sandstone due to the higher K-feldspar abundance.

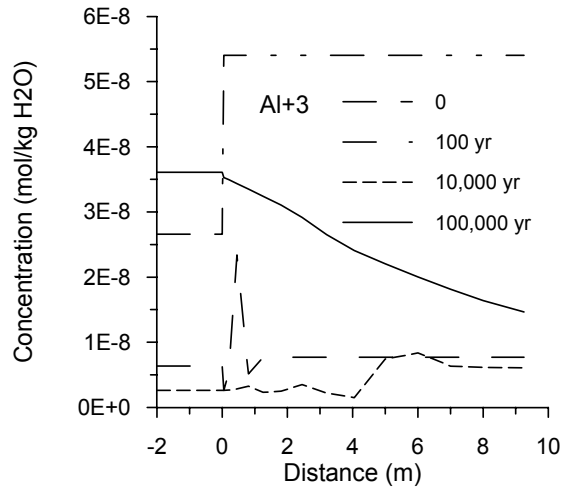

(i)

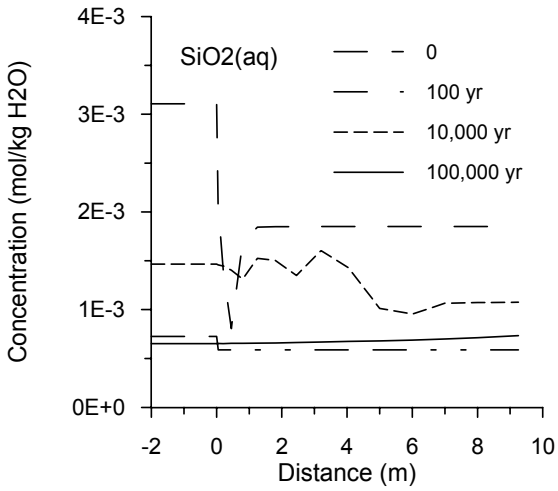

(j)

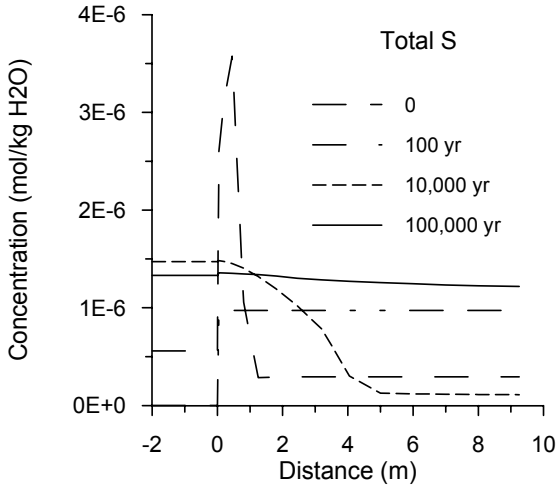

(k)

Figure 2. (Continued). (i and j) Al^{+3} and SiO_2(aq) concentrations are controlled by the dissolution and precipitation of a number of aluminosilicate minerals; (k) Total sulfur concentration is buffered by kerogen-OS dissolution and pyrite precipitation.

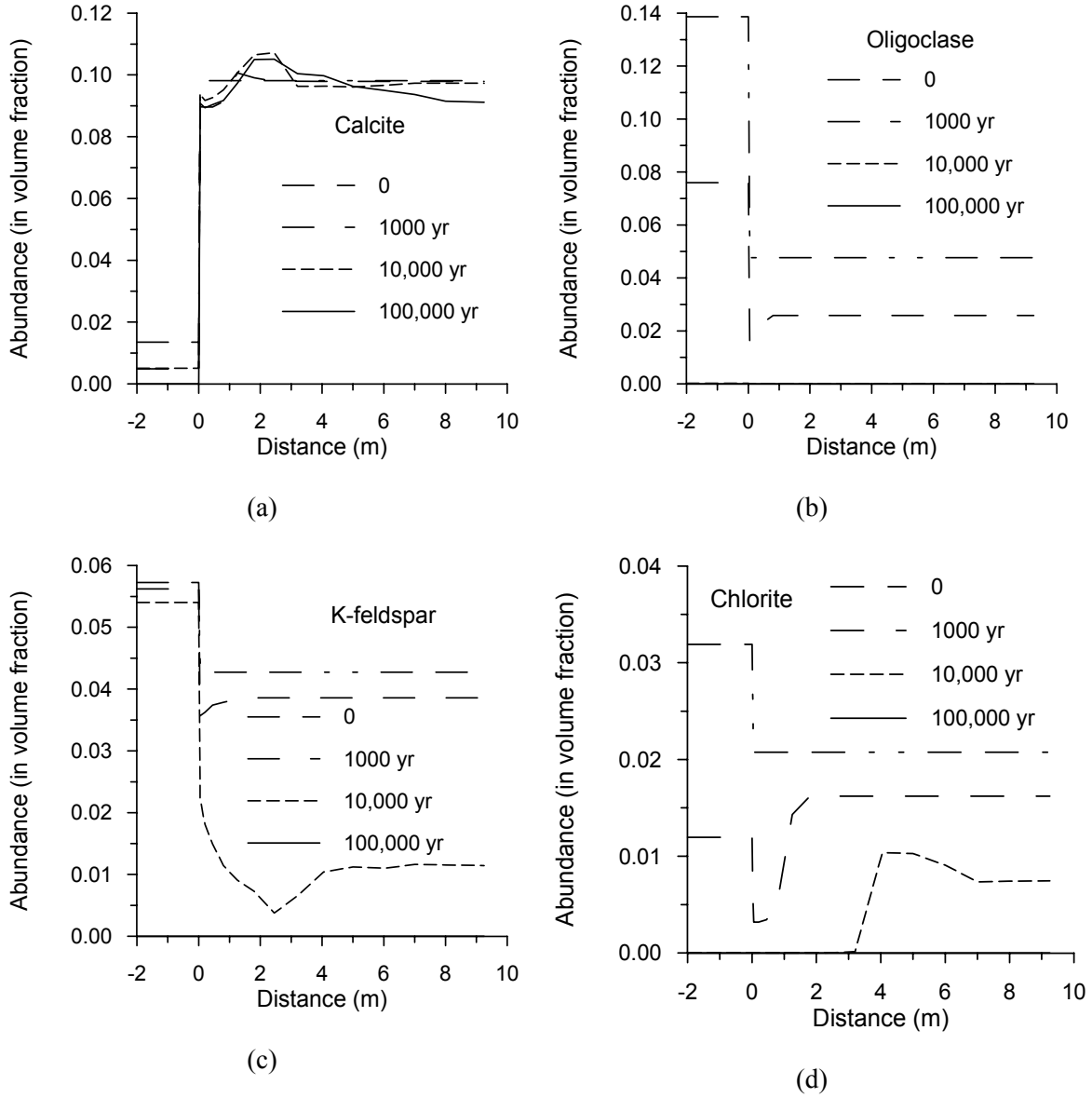

Figure 3. Mineral abundances (in volume dimensionless fraction) along the sandstone-shale transect. (a) Significant dissolution of calcite occurs in the sandstone due to lower pH in the presence of high CO_2 pressure. Slight dissolution and precipitation of calcite occurs in the interior of the shale; (b) Oligoclase disappears very rapidly between 1,000 and 10,000 yr in both sandstone and shale layers; (c) K-feldspar is destroyed just after 10,000 yr in both layers; (d) Chlorite dissolution also occurs in both layers, it disappears in the sandstone just after 1,000 yr. Some chlorite remains in the interior of the shale at 10,000 yr, but all chlorite has disappeared by 100,000 yr.

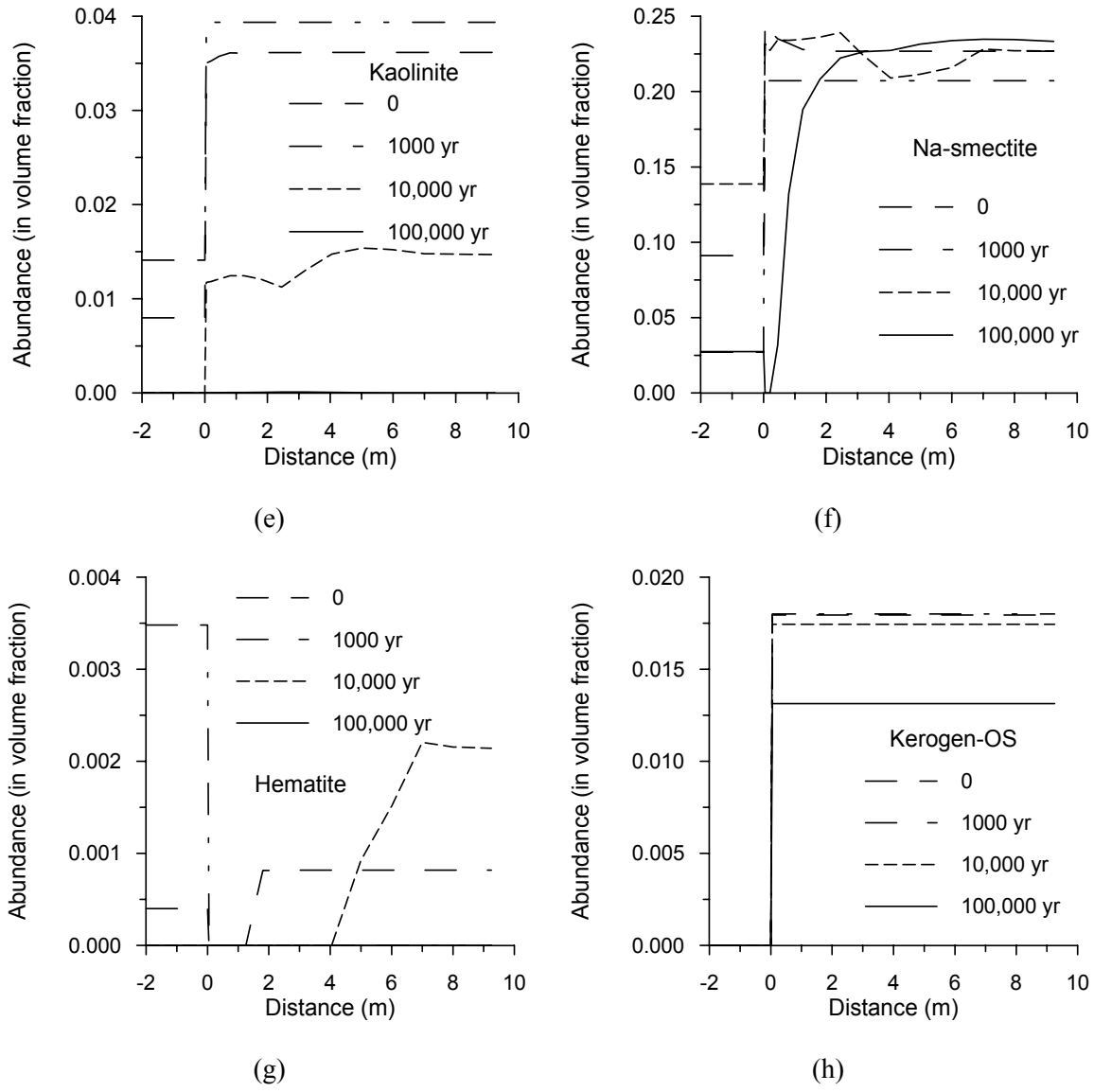

Figure 3. (Continued). (e) Kaolinite dissolves steadily in both layers; (f) Na-smectite dissolution occurs mostly in the sandstone and in the shale close to the interface; (g) Hematite dissolution initially occurs in the sandstone, but later precipitates into the shale interior; (h) Kerogen-OS dissolves steadily and uniformly throughout the shale.

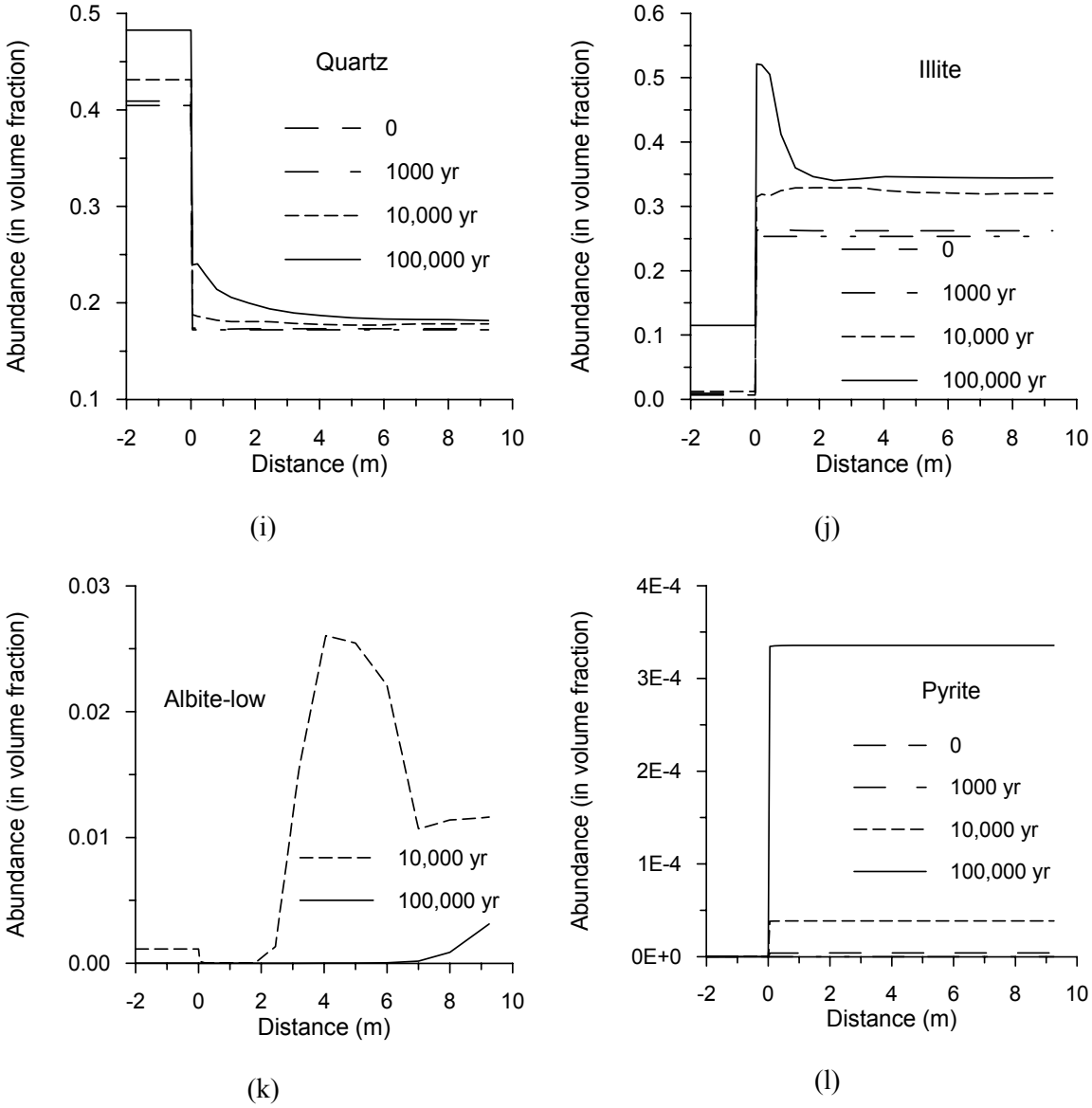

Figure 3. (Continued). (i) Quartz precipitates in the sandstone but remains essentially at equilibrium in the interior of the shale; (j) Illite precipitates due to dissolution of K-feldspar, particularly in the shale close to the sandstone interface; (k) Low-albite precipitation occurs at 10,000 yr in both layers with a maximum concentration at x = 4 m, but later dissolves; (l) Pyrite precipitates steadily in the shale due to the release of sulfide by dissolving kerogen-OS.

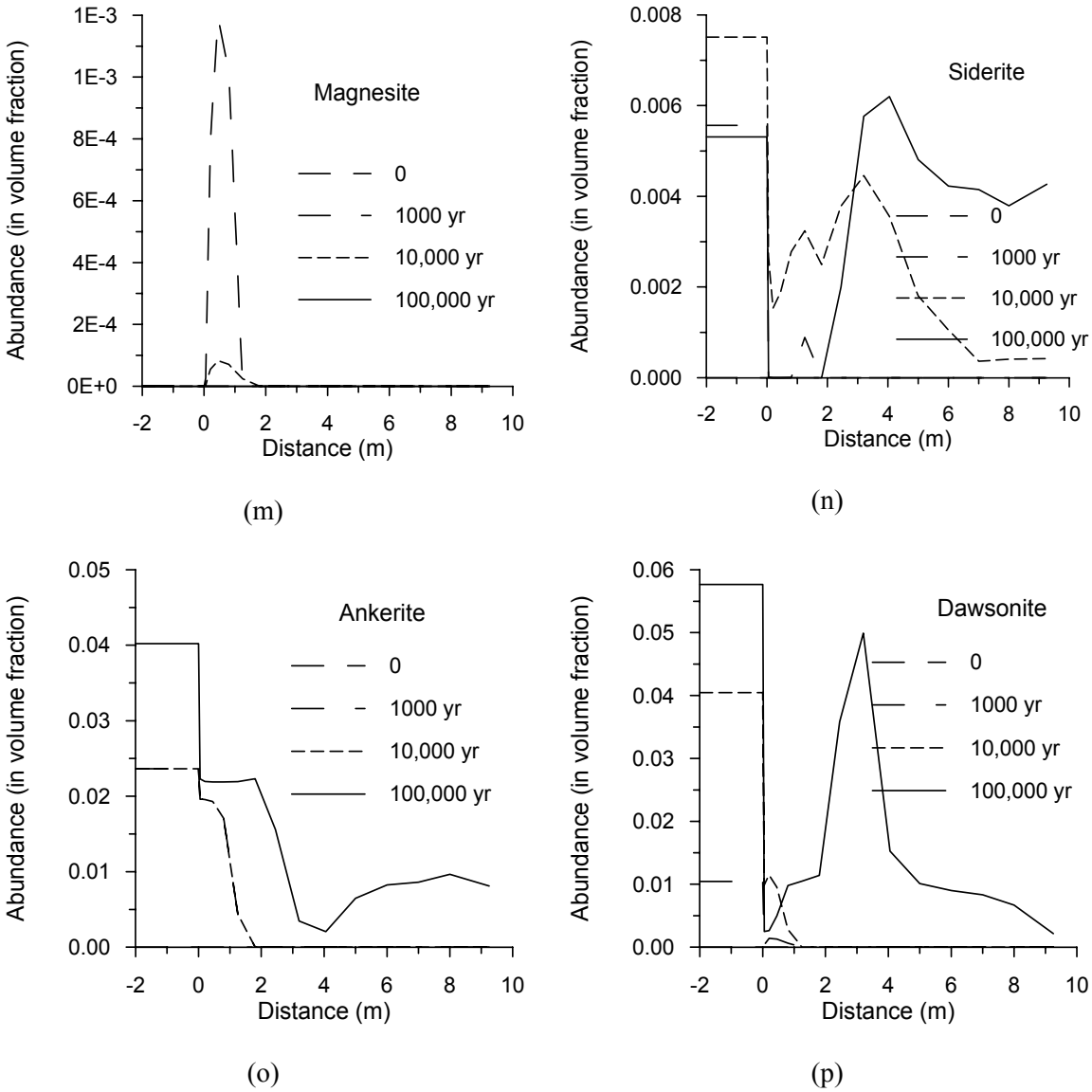

Figure 3. (Continued). (m) Minor magnesite forms close to the interface in the shale between 1,000 and 10,000 yr, but later dissolves completely; (n) Siderite precipitation initially occurs only in the sandstone, but later occurs in the shale due to diffusive transport of CO_2 from the sandstone; (o and p) Significant CO_2 is respectively immobilized by precipitation of ankerite and dawsonite. After 100,000 years a maximum of approximately 4% and 6% of volume fraction respectively of ankerite and dawsonite are formed in the sandstone.

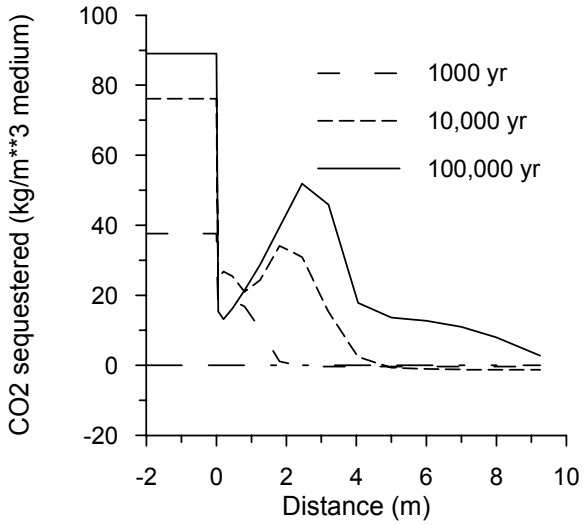

Figure 4. Cumulative CO_2 sequestered by carbonate mineral precipitation along the sandstone-shale transect.

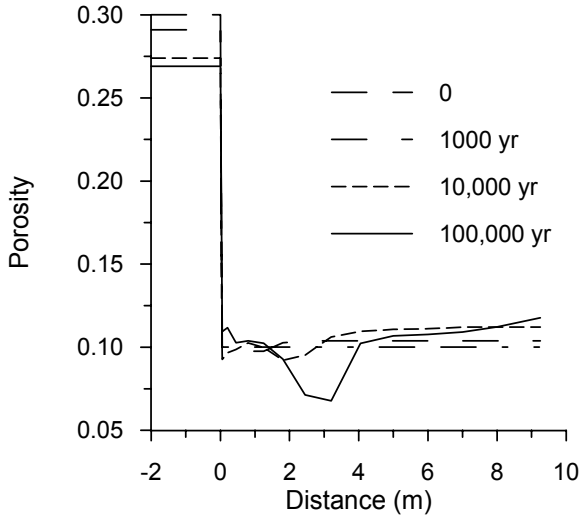

Figure 5. Porosity distribution along the sandstone-shale transect. Precipitation of carbonate minerals results in a decrease of porosity, which is consistent with CO_2 mineral sequestration shown in Figure 4. A slight increase in porosity can be observed in the interior of the shale, indicating the leaching of chemical constituents.

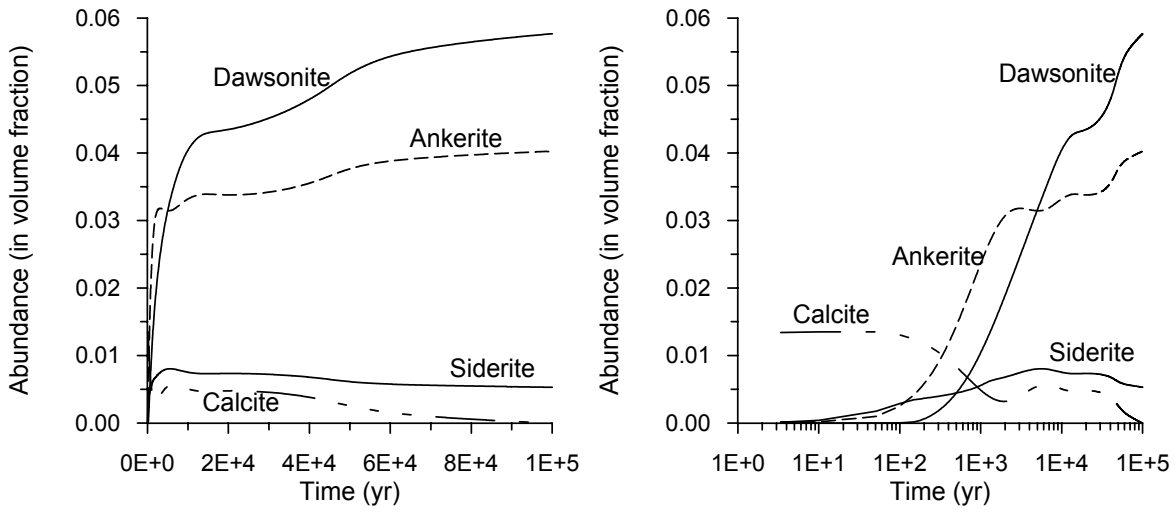

(a) Linear scale (b) Log10 scale

Figure 6. Abundances of carbonate minerals over time in the sandstone. Some CO_2 is immobilized by precipitation of siderite, but more significant by precipitation of ankerite and dawsonite. Precipitation of carbonate minerals occurs primarily before 10,000 yr (a). To emphasize the evolution at initial times, we use a log10 scale for time (b).

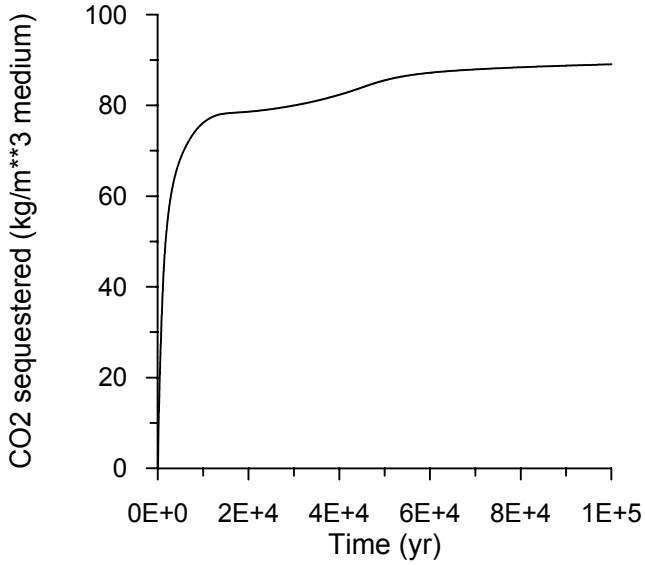

Figure 7. Cumulative CO_2 mineral sequestration over time in the sandstone. Most carbonate minerals precipitate before 10,000 yr consistent with Figure 6.

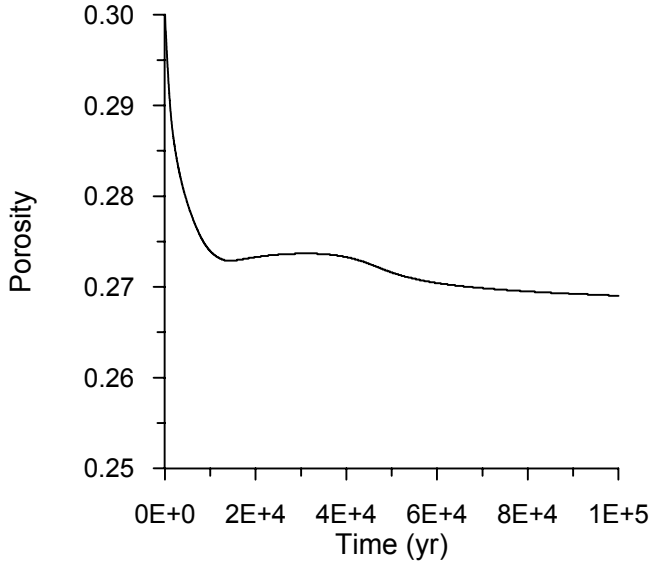

Figure 8. Porosity vs. time in the sandstone. Precipitation of carbonate minerals results in a decrease in porosity, which is consistent with CO_2 mineral sequestration shown in Figure 7.

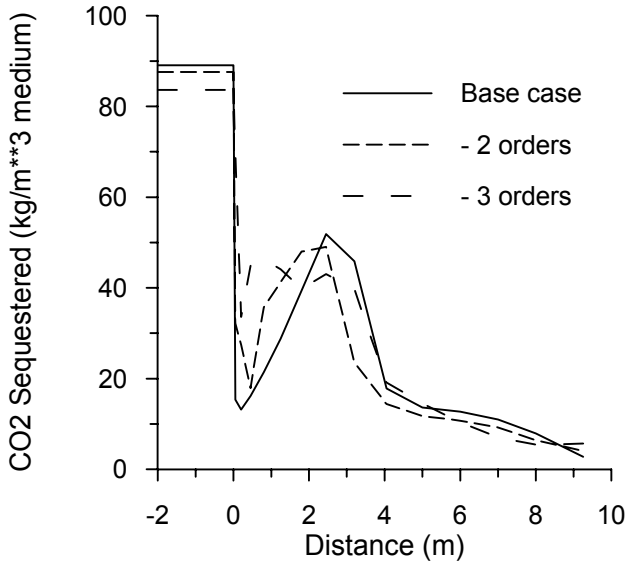

Figure 9. Cumulative CO_2 mineral sequestration after 100,000 years along the sandstone-shale transect obtained by decreasing the dawsonite kinetic rate constant. The total CO_2 sequestered in the sandstone decreases slightly with the rate constant. The total amount of CO_2 sequestered in the shale is very close to the base case except that the peak concentration is located closer to the sandstone interface.

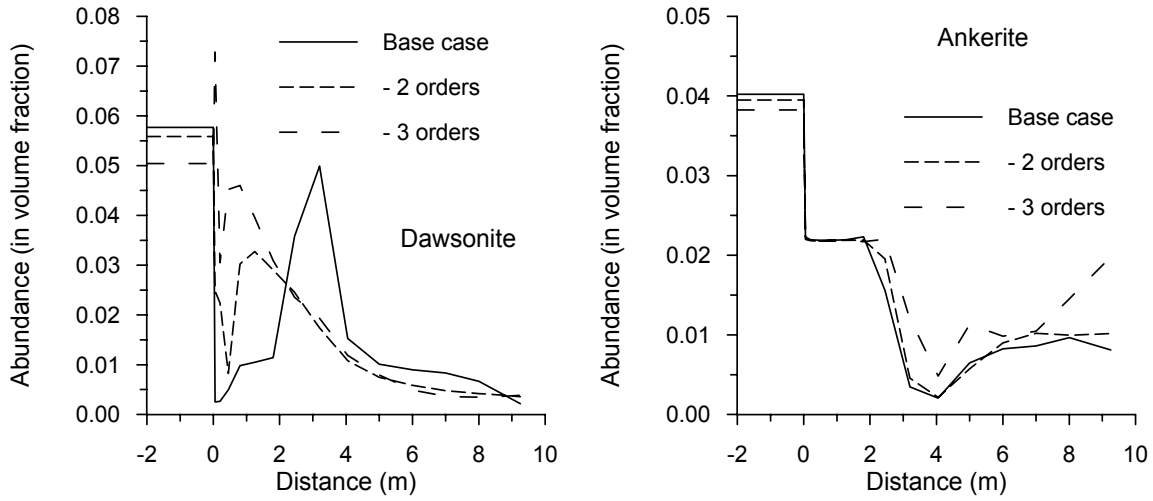

Figure 10. Abundance (in volume fraction) of dawsonite and ankerite along the sandstone-shale transect obtained by decreasing the dawsonite kinetic rate constant by two and three orders of magnitude from the base value (k_{25} = 1.2589×10^{-9} moles m^{-2}s^{-1} in Table 1).

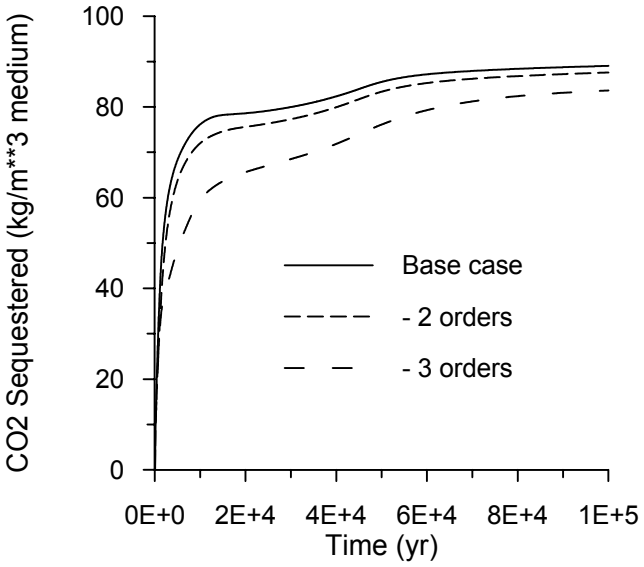

Figure 11. . Cumulative CO_2 mineral sequestration vs. time in the sandstone layer obtained by decreasing dawsonite kinetic rate constant.

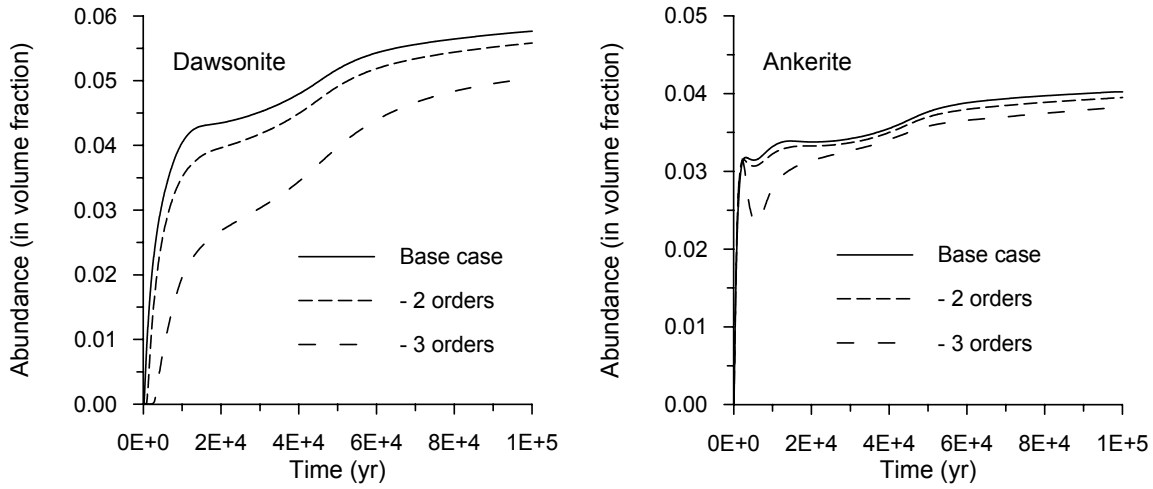

Figure 12. Mineral abundance (in volume fraction) vs. time in the sandstone layer obtained by decreasing dawsonite kinetic rate constant.